Influence of noise on chaotic laser dynamics

Clif Liu,[1] Rajarshi Roy,[2] Henry D. I. Abarbanel,[1,3] Zelda Gills,[2] and Ken Nunes[1,4]
[1]*Department of Physics and Institute for Nonlinear Science, University of California, San Diego, La Jolla, California 92093*
[2]*School of Physics, Georgia Institute of Technology, Atlanta, Georgia 30332*
[3]*Marine Physical Laboratory, Scripps Institution of Oceanography, University of California, San Diego, La Jolla, California 92093*
[4]*Department of Physics, University of California, Santa Cruz, California 95064*
(Received 7 August 1996; revised manuscript received 6 December 1996)

The Nd:YAG laser with an intracavity second harmonic generating crystal is a versatile test bed for concepts of nonlinear time series analysis as well as for techniques that have been developed for control of chaotic systems. Quantitative comparisons of experimentally measured time series of the infrared light intensity are made with numerically computed time series from a model derived here from basic principles. These comparisons utilize measures that help to distinguish between low and high dimensional dynamics and thus enhance our understanding of the influence of noise sources on the emitted laser light.
[S1063-651X(97)10805-4]

PACS number(s): 05.45.+b, 42.50.Lc, 42.65.Sf

I. INTRODUCTION

The Nd:YAG (neodymium doped yttrium aluminum garnet) laser with an intracavity KTP (potassium titanyl phosphate) crystal is a chaotic dynamical system for which it is possible to directly compare statistical aspects of measured time series with predictions from a numerical model that has been derived from basic theory. When operated with three or more longitudinal cavity modes, this laser is known to display chaos, and attempts have previously been made to write dynamical equations that could capture certain aspects of observed behavior [1–3]. These models have successfully predicted the existence of antiphase dynamical states, energy sharing of chaotic polarization modes of the laser, and also the possibility of obtaining stable operation through rotational orientation of the KTP and YAG crystals. The laser system has also served as an example of which algorithms for the control of chaotic lasers have been successfully applied, both experimentally and in numerical simulations [4–7].

It was, however, the observation that simple control algorithms failed in certain operating regimes that motivated us in a previous paper to apply methods of nonlinear time series to experimentally recorded intensity time series with the goal of discovering qualitative and quantitative differences in the operating regimes. The laser was thus operated specifically in three longitudinal modes in two polarization configurations by careful adjustment of crystal orientations in the cavity. In the first configuration, all three longitudinal modes were polarized parallel to each other. In the second, one mode was polarized orthogonal to the other two. All other parameters of the laser system such as the cavity loss, pump level, etc. were maintained constant, and the instrumentation for the measurements was operated with exactly the same sampling times and other settings.

The dynamics observed in these two polarization configurations were labeled type I and type II. Nonlinear time series analysis allowed us to determine the dimensionality of the chaotic attractors for the two cases and estimate the Lyapunov exponents in the two cases. A major conclusion of our previous study was that while the type I behavior was established to be low dimensional, there was clear evidence that the type II behavior was significantly influenced by noise, indicating the presence of high dimensional dynamics as well. At the end of that paper we sketched the outline of a theoretical approach to the derivation of a model that would allow us to simulate intensity time series and apply the nonlinear analysis techniques to make a direct comparison with the experimental results.

In this paper we present the derivation outlined in [8], and obtain the equations that describe the dynamics of a three mode laser with an intracavity KTP crystal. Previous models [1–3] were found not to reproduce type I dynamical behavior after conducting extensive searches in parameter space. It is shown here that the inclusion of nondegenerate four wave mixing, which leads to a model that includes the phase dynamics of the electric fields, overcomes this difficulty. Type II behavior of the infrared light has very different characteristics, and is accompanied by emission of substantial amounts of green light, in contrast to type I dynamics. Degenerate four wave mixing is the dominant process in this case. A major purpose of the research reported here is to include noise sources appropriately in the numerical equations and to explore their influence on type I and type II deterministic chaotic dynamics.

The next section reviews the main aspects of type I and type II chaotic dynamics of the laser. The experimentally observed differences (time series behavior, controllability, mode structure, and green output power) are summarized. We describe a noise measurement method called false nearest neighbors, an algorithm normally used to find the embedding dimension of a chaotic time series. We demonstrate that the two types of dynamics differ significantly in the amount of high dimensional (noisy) dynamics of the laser. Section II provides the basis for comparison with numerical computations that are the focus of this paper.

Section III contains a derivation of the model equations of motion from a Hamiltonian. Three infrared cavity modes are modeled as harmonic oscillators coupled to heat baths. A mode that represents green light generated by the KTP crys-

tal is also included. It is nonlinearly coupled to the infrared modes so as to model the interaction in the KTP crystal. The cavity loss for the green light is very high compared to that for the infrared modes, hence it is sufficient to just consider a single mode of green light and to eliminate its dynamics from the final set of equations that describe the evolution of the field amplitudes of the infrared modes and of the population inversion of the two level atoms that drive them.

In Sec. IV we describe the results from numerically integrating the equations of motion derived in Sec. III. There is a qualitative match between the wave forms of the model and experimental data in both chaos regimes. We also present the false neighbors results when noise is added to the system and find that the resulting noise in the output intensity differs in the two chaotic regimes for the same input noise, leading us to conclude that the susceptibility of the dynamics to noise differs for the two chaotic behaviors.

Section V attempts to locate the source of noise that is seen in the laser time series. Four intrinsic quantum fluctuation sources (cavity loss of infrared light, cavity loss of green light, intrinsic conversion noise, and spontaneous emission) are analyzed for their expected noise levels. These noise sources are all too weak by many orders of magnitude to contribute the amount of noise evidenced in the laser dynamics. We also consider and eliminate extrinsic pumping fluctuations as the noise source.

II. TYPE I AND TYPE II BEHAVIOR

The basic elements of the laser system are a diode laser pumped Nd:YAG crystal and an intracavity KTP crystal with an output mirror that is highly reflecting at the 1.064 μm line of the Nd:YAG crystal but highly transmitting for the green light [1]. It has been shown that this laser can be configured so that few modes ($\approx 3-10$) are present in the cavity; each mode can have one of two polarizations.

Using the methods of nonlinear time series analysis [8] we are able to distinguish between chaotic behavior where the noise level is very low and situations where the output is still chaotic but substantial noise is also present. The former we call type I chaos; it is observed when all three modes all polarized parallel to each other. The latter we label type II chaos; it is observed when one of the three modes is polarized perpendicular to the other two. Very little green light is generated for type I behavior, which is demonstrably low dimensional chaos, and is controllable by the method of occasional proportional feedback (OPF) [4,5]. Type II chaos is accompanied by the generation of a substantial amount of green light and a clear signature of noise is evident in its chaotic dynamics. It is typically not controlled by OPF.

The laser system displays chaotic intensity output when operated with three or more longitudinal modes. In the present experiments the system parameters were adjusted to obtain three mode operation in the two distinct polarization configurations. An appropriate orientation of the crystal axes allowed us to select these configurations. The pump level, set to about twice the threshold pump power, was similar for the two configurations. The total intensity (the sum of the intensities of each individual mode) was observed with a photodiode having a rise time of less than 1 ns and was sampled using a 100 MHz eight bit digital oscilloscope capable of storing 10^6 samples. In Fig. 1(a) we show the total intensity when all three modes are polarized parallel to each other (type I chaos). In Fig. 1(b) we show the total intensity with one mode polarized perpendicular to the other two (type II chaos).

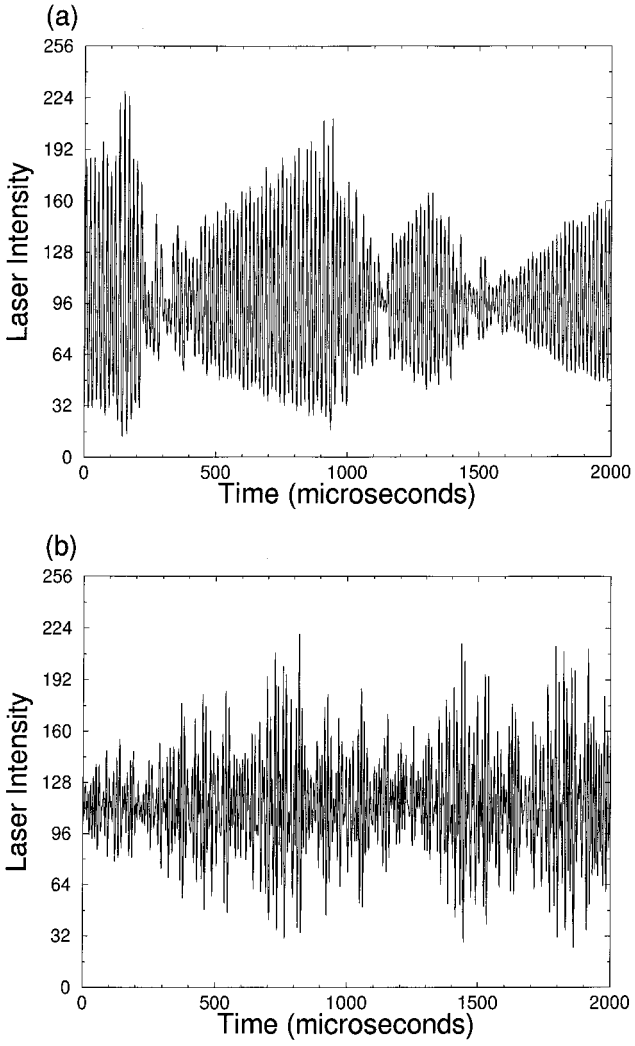

FIG. 1. (a) Fluctuations of the total infrared intensity for three mode Nd:YAG laser operation with all modes polarized parallel to each other. Relaxation oscillations of period ≈ 16 μs are evident with irregular modulations of the envelope, typical of type I dynamics. (b) Fluctuations of the total infrared intensity for three mode Nd:YAG laser operation with two modes polarized parallel to each other and one polarized perpendicular to the other two (type II). The relaxation oscillations are still visible.

In the time traces we can see the distinction between these two operating regimes. Type I consists of long ''bursts'' of relaxation oscillations, while type II appears far more irregular. During type I operation very little green light, less than 1 μW, was observed, while more than 25 μW of power in green light accompanied type II activity.

We use the total laser intensity $I(n)=I(t_0+n\tau_s)$, with the sampling time $\tau_s=100$ ns, and its time delayed values to reconstruct the system phase space [9–12] by forming vectors

$$\mathbf{y}(n)=(I(n),I(n+T),\ldots,I(n+(d_E-1)T)), \qquad (1)$$

$$\mathbf{y}(n+1)=(I(n+1),I(n+1+T),\ldots,I(n+(d_E-1)T+1))$$

$$\vdots \qquad (2)$$

where d_E is the integer embedding dimension of the reconstructed phase space and T is the integer time lag in units of τ_s. Our ability to use this phase space reconstruction for extracting physical properties from the observations rests on a proper choice of the time delay T and the embedding dimension d_E. For T we use the first minimum of the average mutual information [9,10,13] between $I(n)$ and $I(n+T)$ evaluated as a function of T.

d_E is chosen by using the false nearest neighbors algorithm [14,9,10]. This relies on the property of autonomous dynamical systems that their trajectories in phase space do not cross each other unless the system is observed in a space with too low a dimension. To determine the d_E necessary to unfold the trajectories using time delay coordinates we observe each point along the trajectory $\mathbf{y}(n)$ and its nearest neighbor as the dimension of the space is increased from d_E to d_E+1. If the point and its nearest neighbor move sufficiently far from each other as the dimension is increased, we conclude they were falsely seen to be nearest neighbors because of projection from a higher dimensional object, the attractor. When the percentage of false nearest neighbors drops to zero, we have established the value of d_E. Here, we use the property of the algorithm that in the presence of noise [9,10], a residual percentage of false nearest neighbors is observed. The amount of residual is a measure of the noise level.

The original data sets of 10^6 points were oversampled. These were down sampled by a factor of 8, resulting in 125 000 data points. Using the time delay suggested by the average mutual information, we evaluated the percentage of false nearest neighbors for types I and II chaos. This percentage averaged over five type I data traces is shown in Fig. 2(a) (solid line) and enlarged in Fig. 2(b). We see that $d_E=5$ where the percentage of false nearest neighbors drops well below 0.5%. The dotted lines in Figs. 2(a) and 2(b) represent the corresponding average over four type II data sets. In these data it is clear that there is a residual number of false neighbors that is not eliminated by going to higher embedding dimensions. We have consistently observed this much larger fraction of residual false nearest neighbors for type II dynamics compared to type I dynamics in the many time series of total intensity from our laser system. In fact, the mean type II residual is ≈ 40 times the mean type I residual at $d_E=6$.

Table I contains a summary of the differences between type I and type II chaos as found from experimental measurements and from the nonlinear analysis of the data.

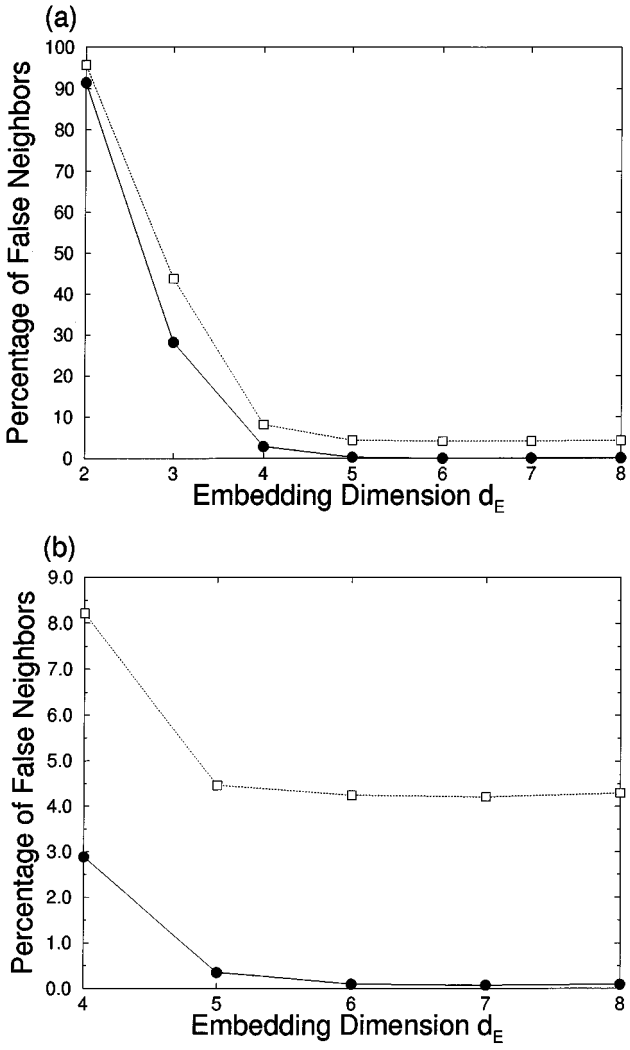

FIG. 2. (a) The percentage of false nearest neighbors (FNN) vs the embedding dimension d_E averaged over five type I chaotic data sets (solid line) and four type II chaotic data sets (broken line). (b) An enlargement of (a) showing that the percentage of type I FNN drops to 0.1% and stays there as d_E increases but the percentage of type II FNN does not drop below 4%.

III. MODEL OF THE PROCESS

The laser is modeled using three interacting components: the infrared cavity modes, a green cavity mode, and a two level active medium. We write the whole Hamiltonian as

$$H=H_{\mathrm{IR}}+H_{\mathrm{green}}+H_{\mathrm{conv}}+H_{2\ \mathrm{level}}+H_{\mathrm{driving}}. \qquad (3)$$

H_{conv} models the conversion of IR to green and vice versa that occurs in the KTP crystal, and H_{driving} models the interaction of the two level system with the infrared cavity modes.

The longitudinal infrared normal modes in the laser are represented by the annihilation and creation operators a_n and $a_n^\dagger$, respectively. These satisfy the usual equal time Bose commutation relations

TABLE I. Type I and type II chaos summary.

Characteristic	Type I	Type II
Time series	Bursting	Irregular
Green output	$<1\ \mu$W	$\geqslant 25\ \mu$W
Mode configuration	3-0	2-1
OPF controllable	Yes	No
Embedding dimension	≈ 5	≈ 5
False neighbors residual	$<1\%$	$\approx 5\%$

$$[a_n, a_m^\dagger] = \delta_{mn}, \quad n,m = 1,2,\ldots,M. \tag{4}$$

For us, $M=3$.

Each mode is coupled to independent heat baths or reservoirs which are represented by boson operators b_{ik} for the kth reservoir mode of infrared mode i. This harmonic oscillator has a frequency of Ω_{ik}. We assume that all of the reservoir modes are independent of each other and the infrared modes (except through the coupling), that is

$$[b_{qn}, b_{pm}^\dagger] = \delta_{mn}\delta_{pq} \tag{5}$$

and

$$[b_{pn}, a_m^\dagger] = 0. \tag{6}$$

The reservoir modes are bilinearly coupled to the infrared modes with real coupling constants Γ_{ik}, which leads to

$$H_{\mathrm{IR}} = \sum_{i=1}^{M} \hbar\omega_i a_i^\dagger a_i + \sum_{i=1}^{M}\sum_k [\hbar\Omega_{ik} b_{ik}^\dagger b_{ik} + i\hbar\Gamma_{ik}(b_{ik}a_i^\dagger - a_i b_{ik}^\dagger)]. \tag{7}$$

There is a single green mode represented by annihilation and creation operators g and $g^\dagger$ that satisfies

$$[g, g^\dagger] = 1 \tag{8}$$

and

$$[g, a_m^\dagger] = 0. \tag{9}$$

It is bilinearly coupled (via real coupling constants Γ_{gk}) to a reservoir that is independent of the infrared mode reservoirs. The kth reservoir mode of the green mode is represented as b_{gk} and has a frequency of Ω_{gk}. The green mode Hamiltonian is

$$H_{\mathrm{green}} = \hbar\omega_g g^\dagger g + \sum_k [\hbar\Omega_{gk} b_{gk}^\dagger b_{gk} + i\hbar\Gamma_{gk}(b_{gk}g^\dagger - g b_{gk}^\dagger)]. \tag{10}$$

In the KTP frequency conversion process, modeled by H_{conv}, conversion occurs when two infrared photons are destroyed to create a green photon and when one green photon is destroyed to create two infrared photons. We assume the coupling tensor κ_{ij} is real and symmetric:

$$H_{\mathrm{conv}} = i\hbar \sum_{i,j=1}^{M} \kappa_{ij}(a_i^\dagger a_j^\dagger g - g^\dagger a_j a_i). \tag{11}$$

The laser driving system is represented by a distribution of spin-1/2 systems along the z axis over the length of the laser cavity. The Pauli spin operators $S_3(z,t)$ and $S_\pm(z,t)$ are used to represent the two level systems and satisfy

$$[S_3(z), S_\pm(z')] = \pm 2 S_\pm(z)\,\delta(z-z') \tag{12}$$

and

$$[S_+(z), S_-(z')] = S_3(z)\,\delta(z-z'). \tag{13}$$

In addition, it can be shown that

$$S_\pm(z)S_3(z') = \mp S_\pm(z)\,\delta(z-z'),$$
$$S_+(z)S_-(z') = \tfrac{1}{2}[I + S_3(z)]\,\delta(z-z'). \tag{14}$$

The two level system is damped by a cavity mode reservoir represented by boson operators b_{sk} and $b_{sk}^\dagger$. The Hamiltonian is

$$H_{2\,\mathrm{level}} = \int_0^L \left\{ \frac{\hbar\omega_s}{2} S_3(z) + \sum_k [i\hbar\Gamma_{sk}(z)S_+(z)b_{sk} - i\hbar\Gamma_{sk}^*(z)b_{sk}^\dagger S_-(z)] \right\} dz + \sum_k \hbar\Omega_{sk} b_{sk}^\dagger b_{sk}. \tag{15}$$

The coupling between the medium and the cavity modes is bilinear and the driving efficiency σ_i is assumed to be real:

$$H_{\mathrm{driving}} = \int_0^L i\hbar \sum_{i=1}^{M} \sigma_i [S_+(z)a_i \sin(K_i z) - a_i^\dagger S_-(z)\sin(K_i z)]dz. \tag{16}$$

A derivation of the equations of motion for this system can be found in the Appendix. Here we give an overview of the physics of the model and the approximations that are made in the derivation.

First we use the Hamiltonian to determine the standard Heisenberg equations of motion for the system. The reservoir model allows us to apply the Wigner-Weisskopf approximation (see Appendix and Chap. 19.2 of [15]) to write a Langevin equation for the green mode:

$$\frac{dg}{dt} = -(\gamma_g + i\omega_g)g - \sum_{lm=1}^{M} \kappa_{lm}^* a_l a_m - \sum_k \Gamma_{gk} b_{gk}(0) e^{-i\Omega_{gk}t}, \tag{17}$$

where γ_g represents the damping rate and the last term is a fluctuation or noise term. Integrating this equation and taking advantage of the fact that the decay rate γ_g ($\approx 10^{10}$ Hz) is much faster than the characteristic rate at which g fluctuates (10^5 Hz), we can find an equation for the green mode:

$$g = -\frac{1}{\gamma_g} \sum_{l,m=1}^{M} \kappa_{lm} a_l a_m + \eta_g, \tag{18}$$

where η_g is a dimensionless fluctuation term

$$\eta_g = -\sum_k \frac{\Gamma_{gk} b_{gk}(0)}{\gamma_g + i(\omega_g - \Omega_{gk})} e^{-i\Omega_{gk}t}. \tag{19}$$

The green mode is seen here to be ''slaved'' to the infrared dynamics; namely, $g(t)$ is determined solely in terms of the infrared modes and fluctuations associated with its coupling to the external world. The use of a single green mode operator is justified as the green light escapes from the laser cavity

and its dynamics is not observed. In what follows, we shall see it acts as a damping factor, and the detailed mode structure is not important.

We do the same with the infrared reservoir and infrared equations of motion and substitute in the green evolution equation to get

$$\frac{dA_i}{dt} = -\gamma_i A_i - \frac{2}{\gamma_g}\sum_{j,l,m=1}^{M} \kappa_{ij}\kappa_{lm} A_j^\dagger A_l A_m + 2\sum_{j=1}^{M} A_j^\dagger \eta_g e^{i(\omega_i+\omega_j)t} + \eta_i e^{i\omega_i t} - \int_0^L \sigma_i^* e^{i\omega_i t} S_-(z)\sin(K_i z)dz. \tag{20}$$

The noise (η_i and η_g) and damping (γ_i and γ_g) can be related through a fluctuation-dissipation relation, which we derive in a later section.

Now we turn to the two level system equations of motion. Although the Nd:YAG laser is actually a four level system, this model works well for determining the equations of motion. It fails when computing the spontaneous emission noise power, so we compute this power in another way. In the meanwhile we will ignore all noise contributions from the two level system.

The equations of motion are found again, and we formally integrate the reservoir operators, substitute them into the $S_+(z)$ equation of motion, and make the Langevin approximation to get

$$\frac{dS_+(z)}{dt} = (-\gamma_p + i\omega_s)S_+(z) + \eta_s(z)S_3(z) - \sum_{i=1}^{M} \sigma_i^* a_i^\dagger S_3(z)\sin(K_i z). \tag{21}$$

At this point, we note that the Nd:YAG laser is a class B laser and its polarization decay rate is much higher than γ_s because the polarization of the active medium is affected by the surrounding crystal lattice. For Nd:YAG, γ_s^{-1} is approximately 240 μs. The actual polarization decay time γ_p^{-1} is on the order of 10^{-11} s.

So we substitute the faster decay rate γ_p for γ_s and ignore the associated fluctuations.

In the interaction frame moving at the driving frequency ω_d we find that the driving terms are slaved to the population inversion $S_3(z)$ due to the high polarization decay rate. In a way similar to the method used to determine the green mode equation of motion we determine the driving terms to be

$$\mathcal{S}_+(z) = -\frac{1}{\gamma_p}\sum_{i=1}^{M} \sigma_i a_i^\dagger e^{-i\omega_d t}\sin(K_i z)S_3(z), \tag{22}$$

$$\mathcal{S}_-(z) = -\frac{S_3(z)}{\gamma_p}\sum_{i=1}^{M} \sigma_i a_i e^{i\omega_d t}\sin(K_i z). \tag{23}$$

We now take the $S_3(z)$ equation, substitute the reservoir solutions, and perform the Langevin approximations.

$$\frac{dS_3(z)}{dt} = 2\Lambda - 2\gamma_s[I + S_3(z)] - 2[S_+(z)\eta_s^\dagger(z) - \eta_s(z)S_-(z)] + 2\sum_{i=1}^{M} \sigma_i[S_+(z)a_i + a_i^\dagger S_-(z)]\sin(K_i z). \tag{24}$$

A constant population inversion 2Λ has been added to account for optical pumping. Further manipulations and associating the operator $S_3(z)$ with the population inversion $n(z)$, we find and equation for the population inversion of the laser,

$$\frac{dn(z)}{dt} = -\frac{1}{\tau_f}[n(z) - \overline{n}] - n(z)\sum_{i=1}^{M} 4\frac{\sigma_i^2}{\gamma_p} A_i^\dagger A_i \sin^2(K_i z), \tag{25}$$

where τ_f is the fluorescence decay time of the Nd:YAG medium (240 μs) and $\overline{n}$ is the mean population inversion.

After substituting the driving terms into the field equation we get

$$\frac{dA_i}{dt} = -\gamma_i A_i - \frac{2}{\gamma_g}\sum_{j,l,m=1}^{M} \kappa_{ij}\kappa_{lm} A_j^\dagger A_l A_m + 2\sum_{j=1}^{M} A_j^\dagger \eta_g e^{i(\omega_i+\omega_j)t} + \eta_i e^{i\omega_i t} + \frac{\sigma_i^2}{N\gamma_p}\int_0^L \sin^2(K_i z)n(z)dz A_i. \tag{26}$$

We have identified $n(z)$ here. At this point we recall that the number of photons in the cavity is large (10^9) and treat the quantum mechanical operators A_i and $A_i^\dagger$ as if they are c numbers.

Since we now have a partial differential equation for $n(z)$, we break this equation into the component normal modes as described in detail in [3]. To do this, we define a mode gain G_i as

$$G_i = \frac{2|\sigma_i|^2\tau_c}{N\gamma_p}\int_0^L n(z)\sin^2(K_i z)dz, \tag{27}$$

where τ_c is the round trip cavity time of the laser (0.2 ns). Assuming that $n(z,t)$ separate into time and space components we can write down equations for the mode gains instead of the population inversion. After rescaling the equations so that the electric field has measurable units we obtain

$$\frac{dE_i}{dt} = \frac{1}{2\tau_c}\left[(G_i - \alpha_i)E_i - \epsilon\sum_{j,k,l=1}^{M} \zeta_{ij}\zeta_{lm}E_j^* E_l E_m\right] + 2\kappa\sum_{j=1}^{M} \zeta_{ij}E_j^*\eta_g e^{i(\omega_i+\omega_j)t} + \sqrt{\frac{\hbar\omega_d}{\tau_c}}\eta_i e^{i\omega_i t}. \tag{28}$$

$$\frac{dG_i}{dt} = \frac{1}{\tau_f}\left[\rho_i - G_i\left(1 + \sum_{j=1}^{M} \beta_{ij}|E_j|^2\right)\right]. \tag{29}$$

At this point we make use of an earlier model of the laser [3]:

$$2\tau_c \frac{dE_i}{dt} = (G_i - \alpha_i)E_i - \epsilon g |E_i|^2 E_i - 2\epsilon \sum_{j \neq i} \mu_{ij} |E_j|^2 E_i, \tag{30}$$

$$\tau_f \frac{dG_i}{dt} = \rho_i - G_i \left(1 + \sum_{j=1}^{M} \beta_{ij} |E_j|^2 \right). \tag{31}$$

where $\mu_{ij} = g_c$ if the modes are parallel polarized and $\mu_{ij} = (1 - g_c)$ if the modes are orthogonally polarized. These values of μ_{ij} have been determined in [3] after consideration of the phase-matching conditions for the intracavity KTP crystal in the presence of the polarized modes of the laser field. Notice that Eq. (30) is a special case of Eq. (28) having the terms where $i = k$ and $j = l$ (or $i = l$ and $j = k$). This is called degenerate four wave mixing. Matching coefficients in the degenerate case, we find that $\zeta_{ij} = \sqrt{g_c}$ when modes i and j are parallel polarized and $\zeta_{ij} = \sqrt{1 - g_c}$ when they are perpendicularly polarized.

We expect that the degenerate and nondegenerate four wave mixing rates differ in the different laser configurations. Type I chaos exhibits nondegenerate four wave mixing with little, if any, degenerate four wave mixing. This implies that the green photons never have a chance to leave the cavity before being downconverted to infrared again. The opposite is true for type II chaos where the green photons immediately leave the cavity. In order to separate these two cases, it is necessary to define a four wave mixing tensor ϵ_{ijkl} where

$$\epsilon_{ijkl} \begin{cases} \epsilon_d \zeta_{ij} \zeta_{kl} & \text{if } i = k \text{ and } j = l \\ \epsilon_d \zeta_{ij} \zeta_{kl} & \text{if } i = l \text{ and } j = k \\ \epsilon_n \zeta_{ij} \zeta_{kl} & \text{otherwise.} \end{cases} \tag{32}$$

Here, ϵ_d is the degenerate four wave mixing rate and ϵ_n is the nondegenerate four wave mixing rate. We see that Eq. (28) is a special case where the two rates are identical while Eq. (30) is the case when there is only degenerate four wave mixing and no nondegenerate four wave mixing.

The equations we numerically integrate are

$$\frac{dE_i}{dt} = \frac{1}{2\tau_c} \left[(G_i - \alpha_i)E_i - \sum_{j,k,k=1}^{M} \epsilon_{ijkl} E_j^* E_k E_l \right] + \eta_i', \tag{33}$$

$$\frac{dG_i}{dt} = \frac{1}{\tau_f} \left[\rho_i - G_i \left(1 + \sum_{j=1}^{M} \beta_{ij} |E_j|^2 \right) \right]. \tag{34}$$

In these equations $i = 1,2,\ldots,M$. We have lumped all of the noise terms into the single additive noise term η_i'. This is possible because the multiplicative noise in Eq. (28) is much smaller than the additive noise (see below).

We use the parameters shown in Table II. ϵ_{ijkl} is the four wave mixing efficiency in inverse watts and has a magnitude on the order of 10^{-5} W^{-1}. It depends on the mode configuration and the relative orientations of the Nd:YAG and KTP crystals. β_{ij} is the cross saturation parameter between modes i and j in units of inverse watts. These values are different for type I and type II chaos and are discussed below.

TABLE II. Model parameters.

Parameter	Value	Description
τ_c	0.2 ns	Round trip cavity time
τ_f	240 μs	Fluorescence decay time of Nd:YAG
α	0.01	Cavity loss factor
ϵ_{ijkl}	See Tables III and Tables IV	Four wave mixing efficiency
ρ_i	0.02	Pumping power
β_{ij}	See Tables III and IV	Cross saturation parameter

IV. NUMERICAL INTEGRATION RESULTS

These model equations were numerically integrated using a standard stiff integrator from the Los Alamos CLAMS library with a time step of 100 ns. The reservoir noise η_i was simulated by adding a complex Gaussian offset with a variance of 10^{-4} W to the electric field of each mode between integration steps.

Type I behavior is obtained in numerical integration when all modes are polarized in the same direction and no nondegenerate four wave mixing is present, as shown in Table III.

The absence of degenerate four wave mixing is consistent with the experimental absence of measurable green output. Figure 3(a) shows a type I time trace obtained by numerical integration of the equations. The bursting behavior and the relaxation oscillation period echo the experimental type I data in Fig. 1(a).

An approximation to type II behavior is obtained when degenerate four-wave mixing dominates over nondegenerate four-wave mixing as shown in Table IV.

Note that the factors ζ_{ij} in (32) are all equal regardless of whether mode i and mode j are parallel or perpendicular. The predominance of degenerate four wave mixing is consistent with experiment; with type II behavior we observe a high amount of green output. An example of a type II time trace obtained from numerical integration is shown in Fig. 3(b).

A. Data preparation

In our previous paper [8] we discussed the digital signal processing methods we used to extract more resolution from

TABLE III. Type I model parameters.

Parameter	Type I chaos Condition	Value
ϵ_{ijkl}	$i = k$ and $j = l$	0 W^{-1}
	$i = l$ and $j = k$	0 W^{-1}
	Otherwise	2.1×10^{-6} W^{-1}
β_{ij}	$i = j$	1.0 W^{-1}
	$i \neq j$	0.6 W^{-1}

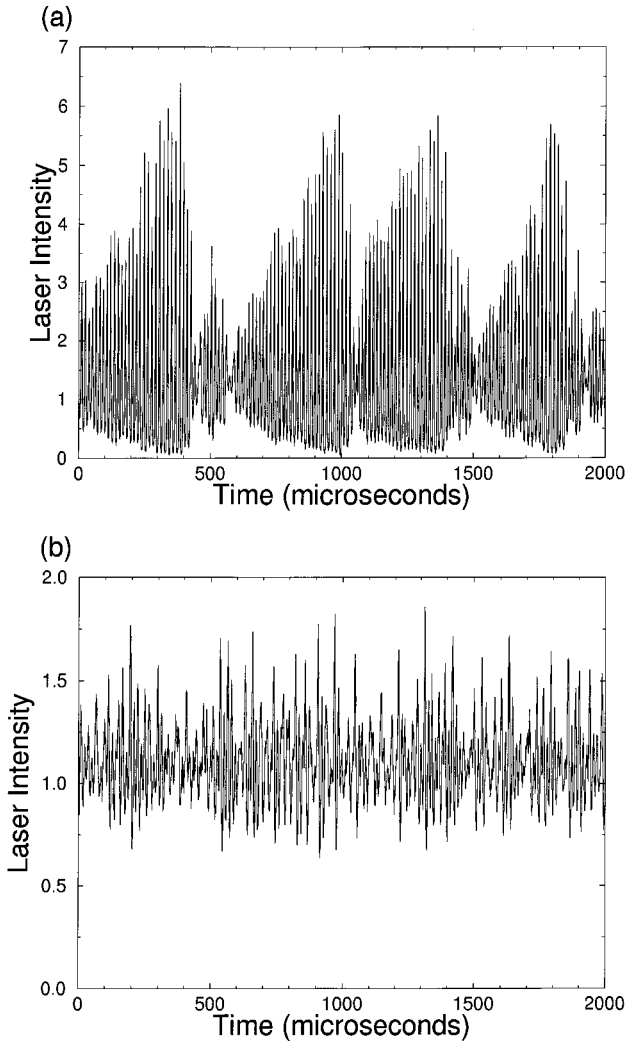

FIG. 3. (a) Numerically integrated type I intensity time series with all modes polarized parallel to each other and no degenerate four-wave mixing. (b) Numerically integrated type II intensity time series with two modes polarized parallel to each other and one polarized perpendicular to the other two and no nondegenerate four wave mixing.

our data acquired using an eight bit sampling oscilloscope. The resolution affects the local false neighbors and the Lyapunov exponent calculations so in order to use these tools to compare the experimental data and the numerical model, it was necessary to perform the same manipulations. In summary, the numerical model was integrated for 10^6 points with a time step of 100 ns, matching the maximum storage capacity and the sampling time of the oscilloscope. The data were then quantized to eight bits. For the false nearest neighbors test and the average mutual information calculation, the data were down sampled by a factor of eight, that is, seven out of every eight samples were thrown out. This leaves 125 000 points at a sampling rate of 1.25 MHz ($\tau_s = 800$ ns). The down sampling preserves the broadband noise level.

TABLE IV. Type II model parameters.

Parameter	Type II chaos Condition	Value
ϵ_{ijkl}	$i=k$ and $j=l$	10^{-5} W^{-1}
	$i=l$ and $j=k$	10^{-5} W^{-1}
	Otherwise	0 W^{-1}
β_{ij}	$i=j$	1.0 W^{-1}
	$i\neq j$	0.85 W^{-1}

For the local false nearest neighbors test and the Lyapunov exponents, the quantized data were interpolated using a digital linear filter. This filter is designed to remove frequencies from 500 kHz to the Nyquist frequency $f_s/2 = 5$ MHz and pass all frequencies below 500 kHz. This was needed to get higher resolution from the experimental data traces. In order to match our results, we did this with the numerical traces as well. After performing the interpolation, the data were also down sampled by a factor of 8, leaving 125 000 points at a sampling rate of 1.25 MHz (800 ns).

B. Power spectrum

When we compare the power spectra of the numerical results and the experimental data, we find similarities. Figure 4 shows the power spectra for the experimental data [Fig. 4(a)] and the numerical data [Fig. 4(b)] for type I chaos. The peaks and their structure are very similar. Figure 5 shows the same information for type II chaos. Here, it is not clear from the spectra whether the type II chaos is well modeled.

C. Average mutual information

The average mutual information of the model is strikingly similar to the experimental data. Figure 6(b) is the average mutual information as a function of time lag for the numerically integrated model for type I chaos, and has essentially the same shape as the average mutual information function of the experimental data [Fig. 6(a)]. Note that the relaxation oscillation time is slightly different between the model and the data, however, this can be adjusted with a small change in the pump power.

The average mutual information function for type II chaos is also very similar between model and experiment as shown in Fig. 7. Again, the relaxation oscillation time can be refined by changing the pumping power.

D. False nearest neighbors

When we examine how the model dynamics respond to noise using the false nearest neighbors algorithm, we find that the type I dynamics tend to suppress noise while the type II dynamics do not. Figure 8 shows the false nearest neighbors results for the numerically integrated time traces (125 000 points) for both types of dynamics, with and without reservoir noise. It is clear, especially in Fig. 8(b) that when no noise is present, both type I and type II dynamics exhibit low-dimensional behavior with almost no residual.

When Gaussian noise ($\sigma = 0.01|\mathcal{E}_{\text{nominal}}|$) is added to the electric field for every integration time step of 100 ns, we find that type I dynamics have no residual, or in other words, the reservoir noise has been suppressed by the dynamics. However, in the type II dynamics, the residual is around 5%, which indicates that the dynamics have been significantly

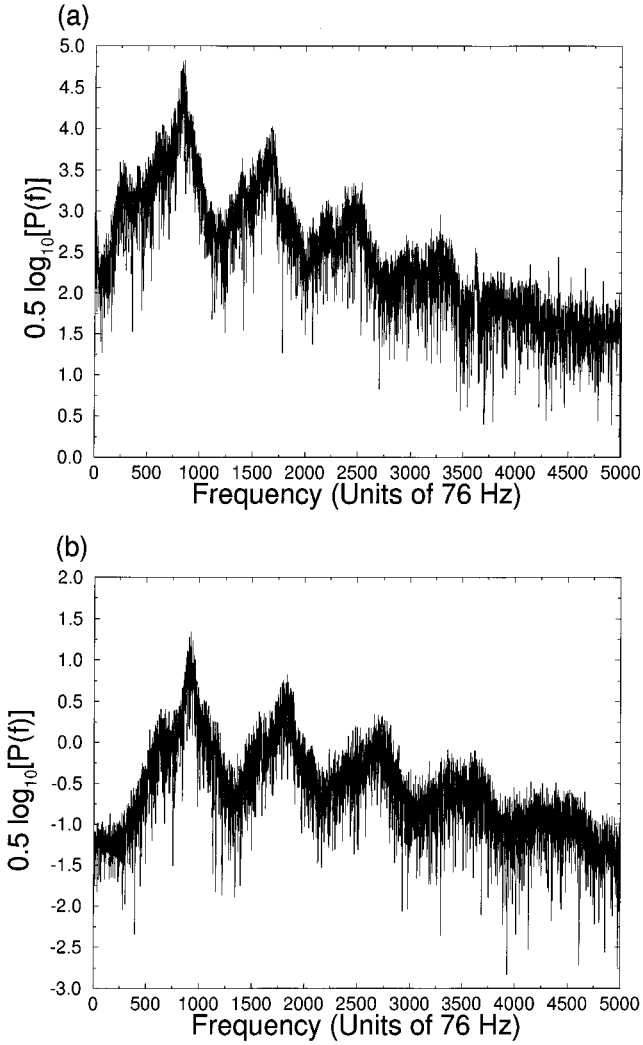

FIG. 4. (a) The power spectrum of the type I experimental data shown in Fig. 1(a). (b) The power spectrum of the numerically integrated time series shown in Fig. 3(a) (type I chaos).

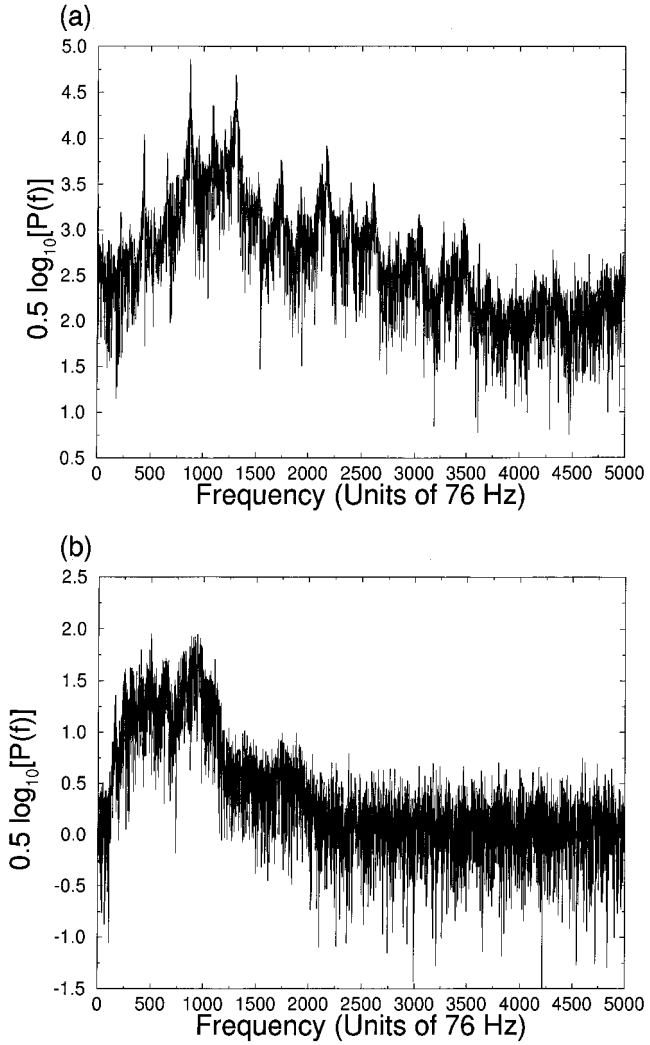

FIG. 5. (a) The power spectrum of the type II experimental data shown in Fig. 1(a). (b) The power spectrum of the numerically integrated time series shown in Fig. 3(b) (type II chaos).

affected by the reservoir noise. These findings are numerically consistent with our observations. When we normalize the noise levels using the maximum amplitude of the type I and type II time series, we find that type II is three times more susceptible to noise than type I.

E. Local false nearest neighbors

We also performed a test called local false nearest neighbors on the numerical data [8]. This is used to find the local dimension, or number of equations of motion of the system that generated the data. The results for type I chaos are shown in Fig. 9. For the experimental data [Fig. 9(a)] the predictability of the data has become independent of the number of neighbors and the embedding dimension. We find that numerical results [Fig. 9(b)] match well; both sets have a local dimension $d_L \approx 6$ and the same fraction of poor predictions. For type II chaos (Fig. 10) the match is not so good—the fraction of poor predictions is different by a factor of 2 and the local dimension appears substantially smaller for the model than for the experiment.

F. Average local Lyapunov exponents

The average local Lyapunov exponents matched well between the model and experimental type I traces. These are computed using the methods described in [8]. Figure 11 shows the average local Lyapunov exponents for the experimental type I data [Fig. 11(a)] and numerical model type I data [Fig. 11(b)] using $d_E = 7$ and $d_L = 7$. Figure 12 shows a closeup of these graphs. Note that in both cases, there are two positive Lyapunov exponents and a zero exponent. The negative Lyapunov exponents are slightly larger for the model dynamics. It is likely that a small parameter change can improve the match.

For the type II data, the match is not so good. Figure 13 shows the average local Lyapunov exponents for the experimental type II data [Figure 13(a)] and the numerical model type II data [Fig. 13(b)] using $d_E = 7$ and $d_L = 7$. Figure 14 is a closeup of these graphs. The experimental data have three positive Lyapunov exponents while the numerical model has 2. The largest Lyapunov exponent from the experimental data exceeds that of the model by a factor of two. We conclude that the model of type II dynamics does not match the experiment well.

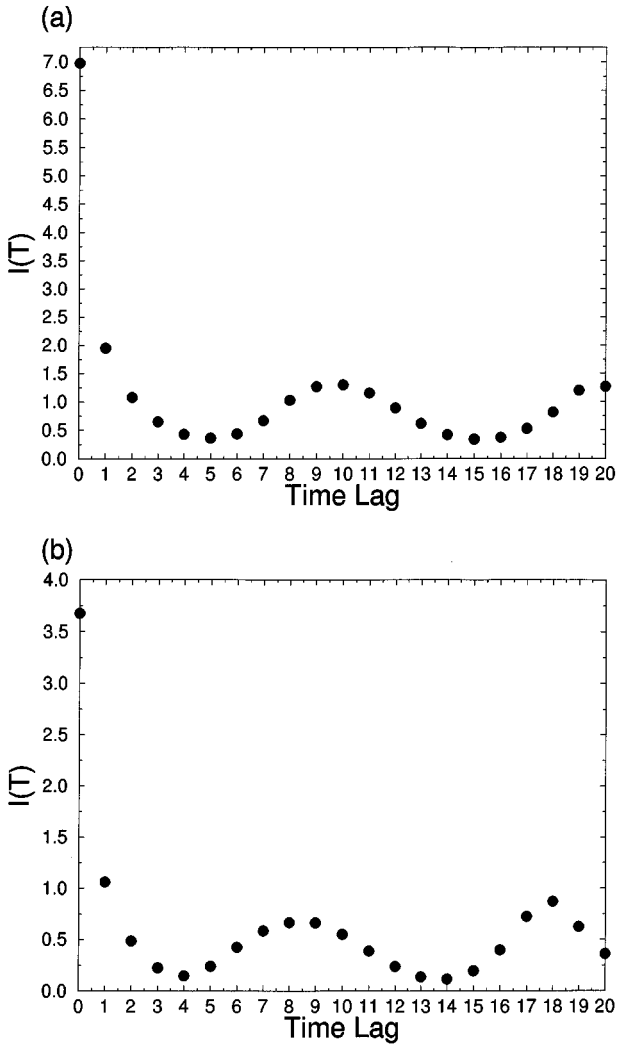

FIG. 6. (a) The average mutual information as a function of time lag for the experimental time series shown in Fig 1(a) (type I chaos). The time lag is given in units of 8/100 MHz or 800 ns. (b) The average mutual information as a function of time lag for the numerically integrated time series shown in Fig. 3(a) (type I chaos).

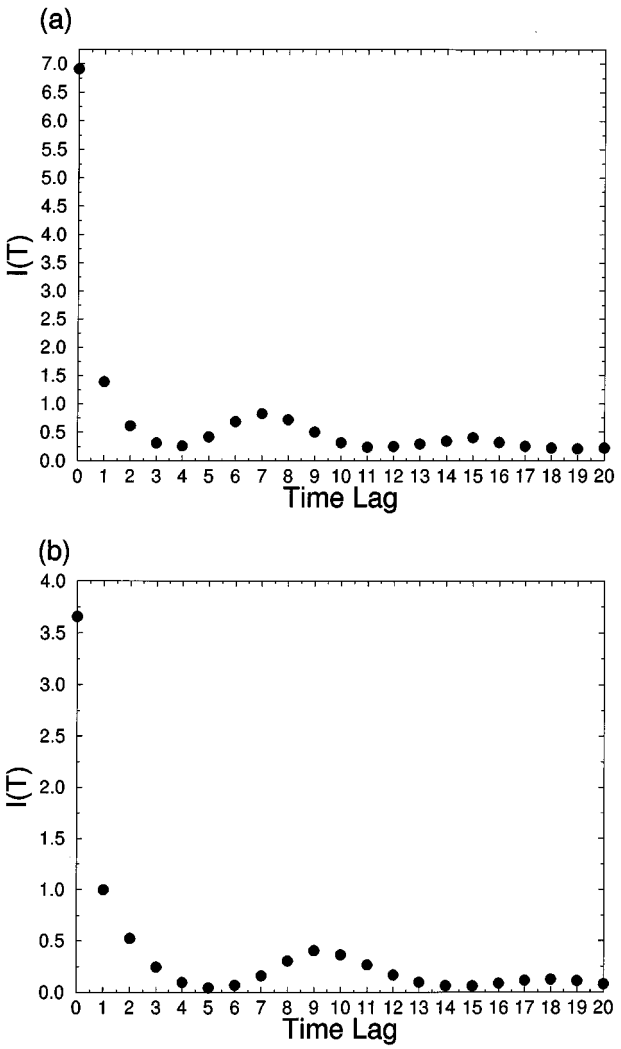

FIG. 7. (a) The average mutual information as a function of time lag for the experimental time series shown in Fig. 1(b) (type II chaos). The time lag is given in units of 8/100 MHz or 800 ns. (b) The average mutual information as a function of time lag for the numerically integrated time series shown in Fig. 3(b) (type II chaos).

Table V gives the average Lyapunov exponent values for $L=2048$, which is a good approximation of the global Lyapunov exponents for the experimental data and the model data. From these numbers, it is clear that type I chaos is modeled well, while type II chaos is not.

V. NOISE SOURCES

In an attempt to determine the source of the noise in the equations, we discuss four sources of intrinsic quantum fluctuations: fluctuations due to cavity damping of the infrared, fluctuations due to the green light leaving the cavity, fluctuations due to spontaneous emission, and fluctuations inherent in the conversion process. We also examined the possibility of fluctuations in the pumping power, and concluded that these could not cause the noise in the output intensity.

We choose to compute the noise levels in photons/s, so we abandon our current units and go back to using the c numbers associated with the creation and annihilation operators $A_i^\dagger$ and A_i. $A_i^\dagger A_i$ is simply the number of photons in mode i and we call this quantity N_{IR}. We repeat the differential equation governing A_i using a generic source of noise $\eta(t)$:

$$\frac{dA_i}{dt} = -\gamma_i A_i - \frac{2}{\gamma_g}\sum_{j,l,m=1}^{M} \kappa_{ij}\kappa_{lm} A_j^\dagger A_l A_m + \sqrt{D}\,\eta, \quad (35)$$

where $\eta(t)$ satisfies

$$\langle \eta^\dagger(t')\,\eta(t)\rangle = \delta(t-t') \quad (36)$$

and D is the noise variance or strength in units of s^{-1}.

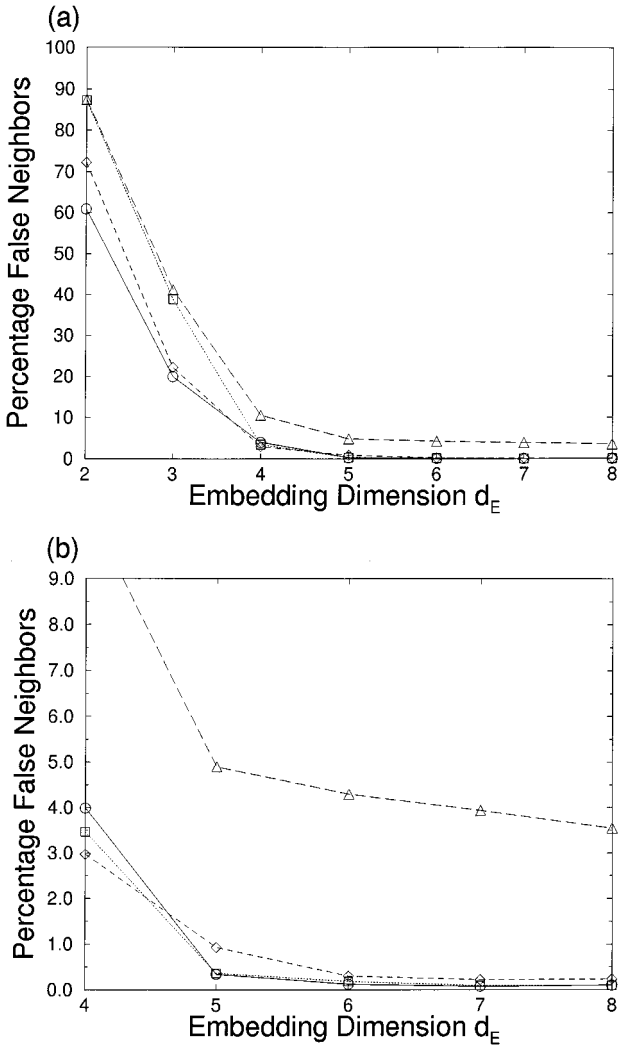

FIG. 8. (a) The percentage of false nearest neighbors (FNN) vs the embedding dimension d_E for the numerically integrated model. The graphs depict type I with no noise (circles), type II with no noise (squares), type I with reservoir noise ($\sigma^2=10^{-4}$, diamonds) and type II with the same reservoir noise (triangle). (b) An enlargement of (a) showing that the percentage of FNN drops to 0.1% and stays there as d_E increases for both types of dynamics with no noise added, and type I dynamics with noise. However, the percentage of type II FNN when noise is added is much higher, around 3% .

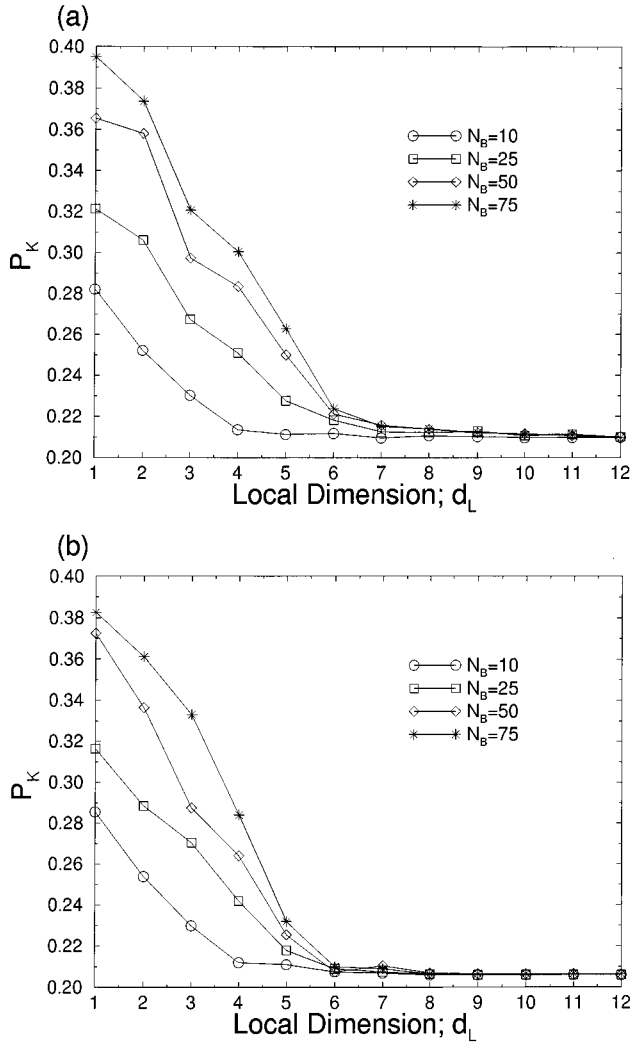

FIG. 9. (a) Local false nearest neighbors for the experimental type I time series shown in Fig. 1(a). (b) Local false nearest neighbors for the numerically integrated type I time series.

The noise power in units of photons/s that is added to each mode can be computed using the number equation:

$$\frac{dA_i^\dagger A_i}{dt} = -2\gamma_i A_i^\dagger A_i - \frac{2}{\gamma_g}\sum_{j,l,m=1}^{M} \kappa_{ij}\kappa_{lm} A_i^\dagger A_j^\dagger A_l A_m + A_i^\dagger \sqrt{D}\,\eta - \frac{2}{\gamma_g}\sum_{j,l,m=1}^{M} \kappa_{ij}\kappa_{lm} A_j A_l^\dagger A_m^\dagger A_i + \sqrt{D}\,\eta^\dagger A_i\,. \tag{37}$$

The amount of noise added to the numerical integration in these units can be determined by converting the noise term in the above equation to real units E where $|E|^2$ is in watts.

$$\frac{dE_i}{dt} = -\gamma_i E_i - \frac{2\tau_c}{\gamma_g \hbar \omega_{dj,l,m=1}}\sum^{M} \kappa_{ij}\kappa_{lm} E_j^* E_l E_m + \sqrt{\frac{\hbar\omega_d}{\tau_c}}\sqrt{D}\,\eta. \tag{38}$$

The noise strength in the simulation is 10^3 W/s. Thus, $D=10^{21}$ s^{-1}. Using Eq. (37) we find that the noise in photons/s is

$$N_{num} \approx 2\sqrt{N_i}\sqrt{D}\frac{1}{\mathrm{s}^{-1/2}}, \tag{39}$$

where N_i is the number of IR photons in mode i. The strange units in Eq. (39) occur because the units of η are the units of a square root of a δ function in time.

From the experiment we find that about 1 mW of infrared light is output from the laser. Given a transmission loss of $\approx 0.1\%$, this means that there is approximately 1 W of infrared power inside the cavity. Since each photon has an energy of $\hbar\omega_d = 2\times 10^{-19}$ J and the round trip cavity time is

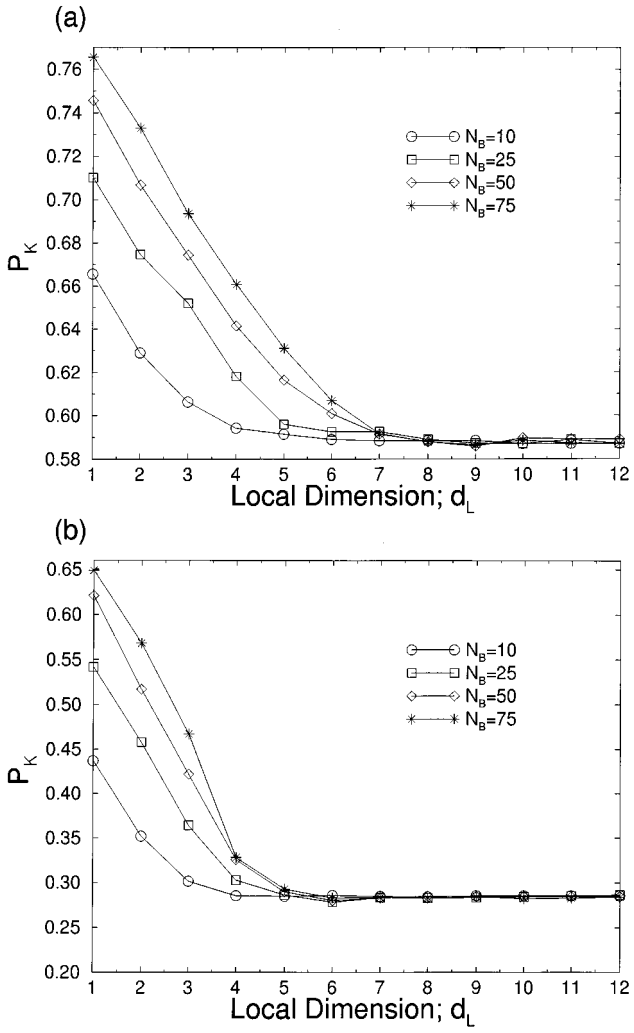

FIG. 10. (a) Local false nearest neighbors for the experimental type II time series shown in Fig. 1(b). (b) Local false nearest neighbors for the numerically integrated type II time series shown in Fig. 3(b).

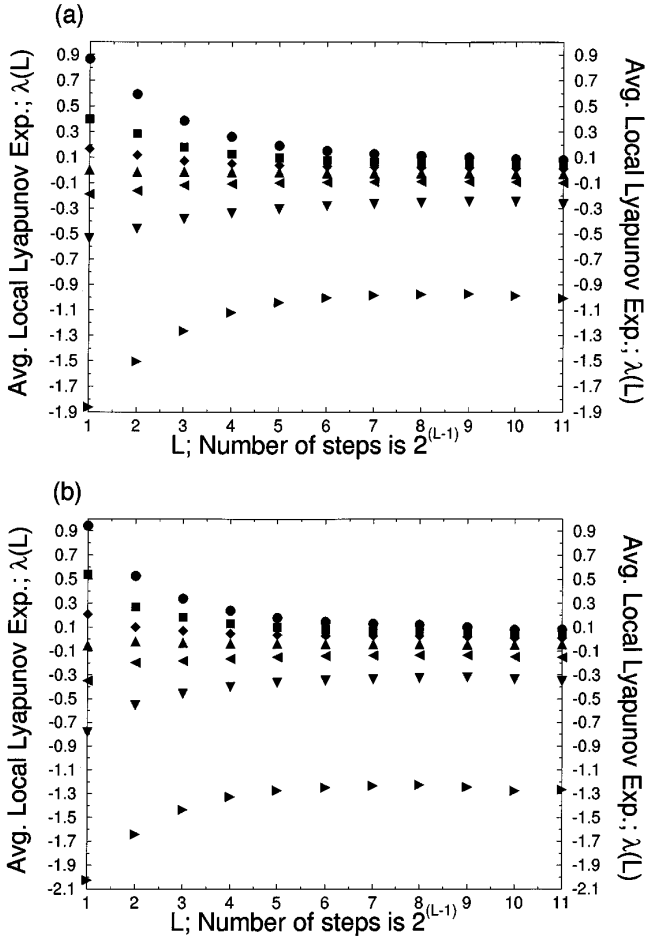

FIG. 11. (a) The average local Lyapunov exponents for the experimental type I time series shown in Fig. 1(a). (b) The average local Lyapunov exponents for the numerically integrated type I time series shown in Fig. 3(a).

$\tau_c = 2\times 10^{-10}$ s, we find that $N_i \approx 10^9$. This puts the numerical integration noise at 2×10^{15} photons/s.

Similarly, the output green power of 100 μW with a fully transmitting cavity implies that the number of green photons in the cavity N_g is about 10^5.

A. Damping fluctuations

First we wish to find the noise power due to damping of infrared light. We compute the noise strength D_{ii}.

$$\langle \eta_i^\dagger(t)\,\eta_i(t')\rangle = D_{ii}\delta(t-t'). \tag{40}$$

Based on Chap. 19-2 in [15] we find that

$$N_i^{\mathrm{IR}} = \gamma_i\langle n(\omega_i)\rangle = \frac{\alpha}{\tau_c}\langle n(\omega_i)\rangle, \tag{41}$$

where $\langle n(\omega_i)\rangle$ is the mean occupation number of bosons and

$$\langle n(\omega_i)\rangle = \frac{1}{e^{\hbar\omega_i/kT}-1}. \tag{42}$$

Here, k is Boltzmann's constant and T is the temperature of the reservoir, which we take to be the cold cavity temperature of 300 K. The energy of an infrared photon is 1.2 eV while kT at room temperature is about 0.026 eV. Thus $\langle n(\omega)\rangle$ is 10^{-20}. The noise strength is 10^{-13} s^{-1}. The noise added to each mode due to IR damping is approximately

$$N_{\mathrm{IR}} \approx 2\sqrt{N_i}\sqrt{D_{ii}} = 0.02 \text{ photons/s}. \tag{43}$$

Similarly, the green noise strength is

$$\langle \eta_g^\dagger(t)\,\eta_g(t')\rangle = D_g\delta(t-t') = \frac{\langle n(\omega_g)\rangle}{\gamma_g}\delta(t-t'). \tag{44}$$

The noise power in infrared mode i due to green cavity damping fluctuations from Eq. (A47) is

$$N_i^{\mathrm{green}} = 2\sum_{j=1}^{M}\kappa_j A_i^\dagger A_j^\dagger\sqrt{D_g}\,\eta + 2\sum_{j=1}^{M}\kappa_j A_j^\dagger A_i^\dagger\sqrt{D_g}\,\eta^\dagger, \tag{45}$$

which we approximate as

$$N_i^{\mathrm{green}} = 4\kappa N_i\sqrt{\frac{\langle n(2\omega_d)\rangle}{\gamma_g}}. \tag{46}$$

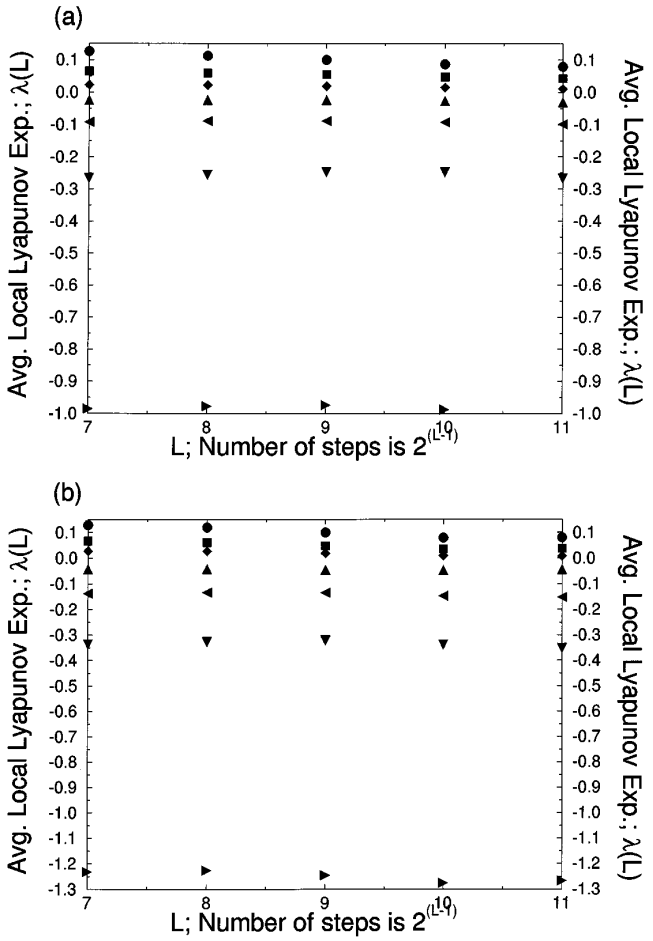

FIG. 12. (a) A closeup of Fig. 11(a). (b) A closeup of Fig. 11(b).

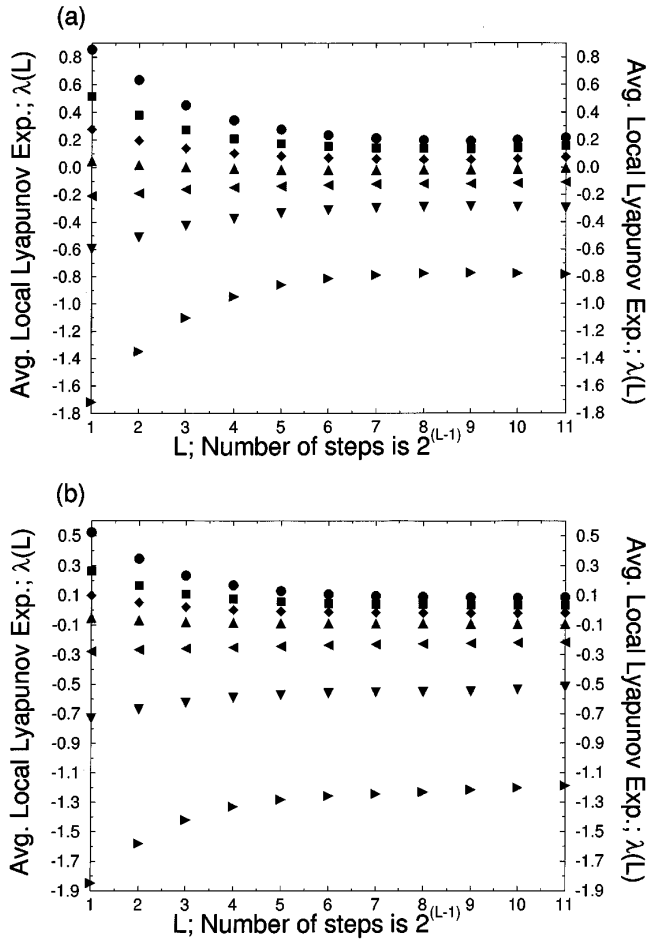

FIG. 13. (a) The average local Lyapunov exponents for the experimental type II time series shown in Fig. 1(b). (b) The average local Lyapunov exponents for the numerically integrated type II time series shown in Fig. 3(b).

Since we know the value of ϵ,

$$\epsilon = \frac{4\tau_c^2\kappa^2}{\hbar\omega_d\gamma_g} \approx 10^{-5}\ \mathrm{W}^{-1}, \tag{47}$$

we find $\kappa \approx 500\ \mathrm{s}^{-1}$. We assume that the decay time of the green is one cavity round trip time, or $1/\tau_c$, which leads to a noise power of 2×10^{-12} photons/s, which is so tiny that it can be ignored.

B. Spontaneous emission noise

The spontaneous emission power can be determined in a similar way to the infrared and green contributions shown above. A simpler method following [16] is used instead.

The Nd:YAG medium has a spontaneous emission spectrum with a Lorentzian shape of width γ_p or 6 cm^{-1} (180 GHz). Knowing the density of photon modes in a cavity with volume V,

$$\frac{dN}{df} = \frac{8\pi V f^2}{c^3}, \tag{48}$$

and assuming a cavity volume of 0.25 cm^3 we find that the number of modes in the spontaneous emission width df is $p = 3\times10^9$.

The total spontaneous emission power in photons/s into a single mode is simply

$$N_i^{\mathrm{spont}} = \frac{N_2}{p\tau_f}, \tag{49}$$

where N_2 is the population of the second level. We can determine this population at threshold especially easily for an Nd:YAG laser because it is a four level laser where $N_2 >> N_1$. According to [16], just below threshold,

$$(N_2 - N_1)_{\mathrm{threshold}} = \frac{p\tau_f}{\tau_p} \approx N_2, \tag{50}$$

where τ_p is the cavity decay time or, using our constants, $\tau_p = \tau_c/\alpha$. What this says is that no net stimulated emission occurs, and the entire population inversion fluoresces at the same rate as the resulting photons leak away. In our laser the population inversion is about 3×10^{15} at threshold.

Substituting the expression for population inversion into the power equation, we find that at threshold,

$$N_i^{\mathrm{spont}} = \frac{\alpha}{\tau_c} = 5\times10^7\ \text{photons/s}. \tag{51}$$

This is still 7 orders of magnitude lower than the levels we expect from numerical integration.

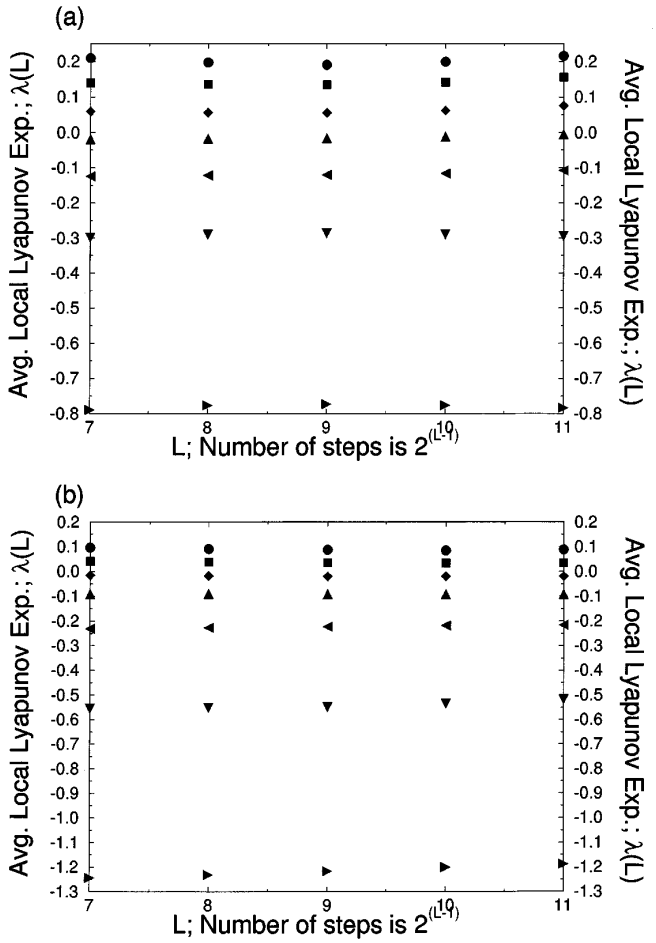

FIG. 14. (a) A closeup of Fig. 13(a). (b) A closeup of Fig. 13(b).

C. Conversion noise

Quantum fluctuations also occur in the conversion of infrared to green and vice versa. This noise must be determined with a different method than used in the above derivation [17,18]. In this calculation, a differential equation is written for the evolution of the density matrix of the system (master equation), a coherent state basis is used to convert the master equation into a Fokker-Planck equation, and finally, the Fokker-Planck equation is converted to a Langevin equation much like Eq. (A47). In the process, a new noise appears, which is related to the diffusion of probability that occurs with nonlinear terms in the Hamiltonian. Since our derivation of this noise term follows [17] almost exactly, we will simply present the results.

TABLE V. Lyapunov exponents of experimental data and model.

Average Lyapunov exponents			
$L = 2048$; $d_E = 7$; $d_L = 7$			
Type 1 chaos		Type 2 Chaos	
Experiment	Model	Experiment	Model
0.080	0.080	0.244	0.088
0.041	0.038	0.172	0.034
0.008	0.009	0.091	−0.019
−0.033	−0.044	0.007	−0.091
−0.102	−0.152	−0.104	−0.216
−0.278	−0.338	−0.298	−0.518
−1.017	−1.266	−0.788	−1.188

Starting with the perturbation related to the KTP conversion process,

$$V = i\hbar \sum_{i,j=1}^{M} \kappa_{ij}(a_i^\dagger a_j^\dagger g - g^\dagger a_j a_i), \tag{52}$$

we find that the terms due to this perturbation in the differential equations are

$$\frac{d}{dt}\begin{bmatrix} \mathcal{A}_1 \\ \mathcal{A}_1^\dagger \\ \mathcal{A}_2 \\ \mathcal{A}_2^\dagger \\ \mathcal{A}_3 \\ \mathcal{A}_3^\dagger \end{bmatrix} = \begin{bmatrix} -2\sum_{j=1}^{3} \kappa_{1j}\mathcal{A}_j^\dagger \mathcal{G} \\ -2\sum_{j=1}^{3} \kappa_{1j}\mathcal{A}_j \mathcal{G}^\dagger \\ -2\sum_{j=1}^{3} \kappa_{2j}\mathcal{A}_j^\dagger \mathcal{G} \\ -2\sum_{j=1}^{3} \kappa_{2j}\mathcal{A}_j \mathcal{G}^\dagger \\ -2\sum_{j=1}^{3} \kappa_{3j}\mathcal{A}_j^\dagger \mathcal{G} \\ -2\sum_{j=1}^{3} \kappa_{3j}\mathcal{A}_j \mathcal{G}^\dagger \end{bmatrix} + \mathbf{B}\begin{bmatrix} \eta_1 \\ \eta_1^\dagger \\ \eta_2 \\ \eta_2^\dagger \\ \eta_3 \\ \eta_3^\dagger \end{bmatrix}, \tag{53}$$

$$\frac{d}{dt}\begin{bmatrix} \mathcal{G} \\ \mathcal{G}^\dagger \end{bmatrix} = \sum_{i,j=1}^{M} \kappa_{ij}\begin{bmatrix} \mathcal{A}_i\mathcal{A}_j \\ \mathcal{A}_i^\dagger \mathcal{A}_j^\dagger \end{bmatrix}. \tag{54}$$

Here, $\mathcal{A}_i$ is a c number similar to (and can be considered to be equivalent to) a_i used earlier. The noise matrix $\mathbf{B}$ is defined by

$$\mathbf{B}\mathbf{B}^T = \begin{bmatrix} \kappa_{11}\mathcal{G} & 0 & \kappa_{12}\mathcal{G} & 0 & \kappa_{13}\mathcal{G} & 0 \\ 0 & \kappa_{11}\mathcal{G}^\dagger & 0 & \kappa_{12}\mathcal{G}^\dagger & 0 & \kappa_{13}\mathcal{G}^\dagger \\ \kappa_{12}\mathcal{G} & 0 & \kappa_{22}\mathcal{G} & 0 & \kappa_{23}\mathcal{G} & 0 \\ 0 & \kappa_{12}\mathcal{G}^\dagger & 0 & \kappa_{22}\mathcal{G}^\dagger & 0 & \kappa_{23}\mathcal{G}^\dagger \\ \kappa_{13}\mathcal{G} & 0 & \kappa_{23}\mathcal{G} & 0 & \kappa_{33}\mathcal{G} & 0 \\ 0 & \kappa_{13}\mathcal{G}^\dagger & 0 & \kappa_{23}\mathcal{G}^\dagger & 0 & \kappa_{33}\mathcal{G}^\dagger \end{bmatrix} \tag{55}$$

and the η terms are zero-mean fluctuation terms satisfying

$$\langle \eta_i^\dagger(t)\,\eta_j^\dagger(t')\rangle = \delta_{ij}\delta(t-t'). \tag{56}$$

Other than the noise term, the four wave mixing perturbations are the same as what were derived earlier. The multiplicative noise term is much larger than the one derived previously. A rough estimate of the number of noise photons added to the IR mode every second is

TABLE VI. Noise power estimates.

Name	Expression	Power	Description
N_i^{green}	$4\kappa N_i\sqrt{\frac{1}{\gamma_g(e^{\hbar\omega_d/kT}-1)}}$	2×10^{-12}/s	Cavity damping of green light
N_i^{IR}	$2\sqrt{N_i}\sqrt{\frac{\alpha}{\tau_c}\frac{1}{e^{\hbar\omega_d/kT}-1}}$	2×10^{-2}/s	Cavity damping of infrared light
N_i^{conv}	$2\sqrt{N_i\kappa N_g}$	10^7/s	KTP frequency conversion
N_i^{spont}	$\frac{\alpha}{\tau_c}$	10^8/s	Spontaneous emission
N_i^{expt}		2×10^{15}/s	Noise power from experiment

$$N_i^{\text{conv}}\approx 2\sqrt{N_i}\sqrt{\kappa N_g} \tag{57}$$

or 10^7 photons/s. This answer can be arrived at by other means. According to Eq. (37) the green production rate is approximately $4\kappa^2 N_i^2/\gamma_g$, which is 2×10^{14} photons/s. This is the mean value of a process whose standard deviation we would expect to be the noise added to the infrared mode. Since the green mode is a coherent state and therefore has a Poisson distribution in the number states, we would expect the standard deviation to be the square root of the mean. Thus, the noise added to the infrared mode should be around 10^7 photons/s. Table VI summarizes the power estimates in photons/s for the noise sources described above.

It appears that there must be another source of noise in our system that contributes much more than these quantum mechanical sources. Pumping fluctuations were considered. To determine if this were the noise source, we substituted

$$\rho_i \Leftarrow \rho_i[1+\sigma\eta(t)] \tag{58}$$

into Eq. (34) where $\eta(t)$ is a zero mean unit variance random number. We found that in order to reproduce the noise levels of the integrated time series with the experimental time series using the false nearest neighbors algorithm, we had to set $\sigma=0.05$ or 5% fluctuation in ρ_i. This level is unrealistically high for pumping fluctuations. In addition, the fluctuations seen in the experimental data have a characteristic frequency that is much higher than the relaxation oscillation rate, which is impossible to attain through pumping fluctuations because of the slow time constant in Eq. (34).

VI. SUMMARY AND CONCLUSIONS

In summary, we have developed a model that captures key features of the intensity dynamics of the three-mode Nd:YAG laser with an intracavity KTP crystal. This model consists of three equations for each infrared mode; two describe the complex electric field and one describes the gain. The inclusion of both degenerate and nondegenerate four wave mixing are features not found in previous models of the laser. Both qualitative and quantitative behaviors found in the experimental system are captured by this model, which is especially successful in its description of the type I case. The distinction between type I and type II chaos is seen as a difference in structure of the four wave mixing tensor, which also leads to a difference in the noise susceptibility of the equations of motion.

Type I chaos occurs when all modes are parallel polarized and is controllable by the OPF chaos control algorithm. The model confirms the bursting behavior found in the time traces. Extremely low levels of green light are measured in type I output, which is described by the model as a predominance of nondegenerate four wave mixing in the laser cavity. Low noise levels are measured in the intensity dynamics, which agrees with the suppression of noise in the type I model dynamics. The local false nearest neighbors test and the Lyapunov exponents match between model and experiment.

Type II chaos occurs when one mode is polarized perpendicular to the other two and is not controllable by the OPF scheme. The spiking, highly irregular time series behavior is captured in the model. The large amount of green light produced by the laser is due to a large amount of degenerate four wave mixing in the laser cavity. The high noise levels found in the intensity dynamics agree with the model's tendency to not suppress reservoir noise but to amplify it instead. However, the local false nearest neighbors test and the Lyapunov exponents do not match well between the model and the experiment, leading us to believe that type II chaos is not fully modeled. We have found that the parameter space of the model is quite complex, especially when degenerate four wave mixing is present. It is possible that additional noise sources remain to be identified and included in the model.

Nonlinear time series analysis has aided this investigation by revealing the link between the high noise levels in the data and the large green light output. A more sophisticated model that reproduces type I behavior almost perfectly and approximates type II behavior is the major result of this paper. Time series analysis allows us to make a quantitative comparison of the model with the experiment. This is the first case we know of where chaotic time series analysis has significantly aided the development of a more complete physical model of the dynamics. This system and model provide a means to study the influence of noise on chaotic systems.

ACKNOWLEDGMENTS

Z.G. and R.R. thank R. Fox, B. Kennedy, and K. Wiesenfeld for many helpful discussions on the material discussed here. Z.G. was financially supported by AT&T. R.R. acknowledges support from NSF Grant No. ECS-9114232. C.L. and H.D.I.A. thank the members of INLS for numerous discussions on this subject. Their work was supported in part by the U.S. Department of Energy, Office of Basic Energy Sciences, Division of Engineering and Geosciences, under Contract No. DE-FG03-90ER14138, and in part by the Office of Naval Research (Contract No. N00014-91-C-0125).

APPENDIX

We reiterate the Hamiltonian:

$$H=\sum_{i=1}^{M}\hbar\omega_i a_i^\dagger a_i+\hbar\omega_g g^\dagger g+i\hbar\sum_{i,j=1}^{M}\kappa_{ij}(a_i^\dagger a_j^\dagger g-g^\dagger a_j a_i)+\sum_{i=1}^{M}\sum_k[\hbar\Omega_{ik}b_{ik}^\dagger b_{ik}+i\hbar\Gamma_{ik}(b_{ik}a_i^\dagger-a_i b_{ik}^\dagger)]+\sum_k[\hbar\Omega_{gk}b_{gk}^\dagger b_{gk}+i\hbar\Gamma_{gk}(b_{gk}g^\dagger$$
$$-gb_{gk}^\dagger)]+\int_0^L\left\{\frac{\hbar\omega_s}{2}S_3(z)+i\hbar\sum_{i=1}^{M}[\sigma_i S_+(z)a_i\sin(K_i z)-\sigma_i^* a_i^\dagger S_-(z)\sin(K_i z)]+\sum_k[i\hbar\Gamma_{sk}(z)S_+(z)b_{sk}-i\hbar\Gamma_{sk}^*(z)b_{sk}^\dagger S_-(z)]\right\}dz$$
$$+\sum_k\hbar\Omega_{sk}b_{sk}^\dagger b_{sk}. \tag{A1}$$

Using this Hamiltonian and the standard Heisenberg equations of motion

$$i\hbar\frac{d\cdot}{dt}=[\cdot,H], \tag{A2}$$

we arrive at the equations of motion governing the system.

$$\frac{da_i}{dt}=-i\omega_i a_i+2\sum_{j=1}^{M}\kappa_{ij}a_j^\dagger g+\sum_k\Gamma_{ik}b_{ik}$$
$$-\int_0^L\sigma_i^* S_-(z)\sin(K_i z)dz, \tag{A3}$$

$$\frac{dg}{dt}=-i\omega_g g-\sum_{l,m=1}^{M}\kappa_{lm}a_l a_m+\sum_k\Gamma_{gk}b_{gk}, \tag{A4}$$

$$\frac{db_{ik}}{dt}=-\Gamma_{ik}a_i-i\Omega_{ik}b_{ik}, \tag{A5}$$

$$\frac{db_{gk}}{dt}=-\Gamma_{gk}g-i\Omega_{gk}b_{gk}. \tag{A6}$$

The green reservoir equation (A6) is linear in $b_{gk}(t)$ so we can integrate it:

$$b_{gk}=-b_{gk}(0)e^{-i\Omega_{gk}t}-\Gamma_{gk}\int_0^t g(t')e^{-i\Omega_{gk}(t-t')}dt'. \tag{A7}$$

Substituting this into (A4) we arrive at

$$\frac{dg}{dt}=-i\omega_g g-\sum_{l,m=1}^{M}\kappa_{lm}a_l a_m+\sum_k\Gamma_{gk}\left[-b_{gk}(0)e^{-i\Omega_{gk}t}\right.$$
$$\left.-\Gamma_{gk}\int_0^t g(t')e^{-i\Omega_{gk}(t-t')}dt'\right]. \tag{A8}$$

The fourth term can be approximated by a damping term using the Wigner-Weisskopf approximation where the modes are assumed to form a continuous spectrum and the interference time of sum on $g(t)$ is assumed to be much smaller than the characteristic time scale of the equation. This approximation is discussed in detail in Sec. 19-2 of [15] and will not be elaborated further here. This leads us to

$$\frac{dg}{dt}=-(\gamma_g+i\omega_g)g-\sum_{lm=1}^{M}\kappa_{lm}^* a_l a_m-\sum_k\Gamma_{gk}b_{gk}(0)e^{-i\Omega_{gk}t}, \tag{A9}$$

where γ_g represents the damping rate.

Since this equation is linear in $g(t)$, we can integrate it to find

$$g=-g(0)e^{-(\gamma_g+i\omega_g)t}$$
$$-\int_0^t\sum_{l,m=1}^{M}\kappa_{lm}a_l(t')a_m(t')e^{-(\gamma_g+i\omega_g)(t-t')}dt'$$
$$-\sum_k\frac{\Gamma_{gk}b_{gk}(0)}{\gamma_g+i(\omega_g-\Omega_{gk})}(e^{(\gamma_g+i\omega_g-i\Omega_{gk})t}-1). \tag{A10}$$

In the integral, we replace the rapidly varying infrared operators $a_i(t)$ with the more slowly varying interaction representation forms $A_i(t)$ in the rotating coordinate system where

$$a_i(t)=e^{-i\omega_i t}A_i(t), \tag{A11}$$

then we perform the integrations by removing the slowly varying operators from under the integral. This method assumes that the damping rate γ_g ($\approx 10^{10}$ Hz) is much higher than the characteristic time scale of the evolution of the slowing varying interaction form of the green operator. We find through experimental observation that the green intensity varies at the same 100 kHz rate as the infrared operator. For times large compared to γ_g^{-1} we can ignore the decaying transients. Thus we find

$$g(t)=-\sum_{l,m=1}^{M}\frac{\kappa_{lm}a_l a_m}{\gamma_g+i(\omega_g-\omega_l-\omega_m)}$$
$$-\sum_k\frac{\Gamma_{gk}b_{gk}(0)}{\gamma_g+i(\omega_g-\Omega_{gk})}e^{-i\Omega_{gk}t}. \tag{A12}$$

This expression is further simplfied if we assume that in order for significant infrared-green conversion to occur, $\omega_g=\omega_l+\omega_m$.

$$g=-\frac{1}{\gamma_g}\sum_{l,m=1}^{M}\kappa_{lm}a_l a_m+\eta_g, \tag{A13}$$

where η_g is a dimensionless fluctuation term

$$\eta_g = -\sum_k \frac{\Gamma_{gk} b_{gk}(0)}{\gamma_g + i(\omega_g - \Omega_{gk})} e^{-i\Omega_{gk}t}. \tag{A14}$$

The green mode is seen here to be ''slaved'' to the infrared dynamics; namely, $g(t)$ is determined solely in terms of the infrared modes and fluctuations associated with its coupling to the external world. The use of a single green mode operator is justified as the green light escapes from the laser cavity and its dynamics is not observed. In what follows, we shall see it acts as a damping factor, and the detailed mode structure is not important.

Performing the same operations on the infrared equations (without the final integration) we arrive at the equations of motion for the M infrared modes.

$$\frac{da_i}{dt} = -(\gamma_i + i\omega_i)a_i + \eta_i - \sum_{j=1}^{M} 2\kappa_{ij} a_j^\dagger g - \int_0^L \sigma_i^* S_-(z)\sin(K_i z)dz, \tag{A15}$$

where

$$\gamma_i = \pi |\Gamma_i(\omega_i)|^2 \mathcal{D}(\omega_i) \tag{A16}$$

$$\eta_i = -\sum_k \Gamma_{ik} b_{ik}(0) e^{-i\Omega_{ik}t}. \tag{A17}$$

$M = 3$ in our problem.

Next we substitute g into this equation, move to a coordinate system rotating with frequency ω_i by substituting

$$A_i = e^{i\omega_i t} a_i, \tag{A18}$$

and assume that in order for significant four wave mixing to occur, $\omega_i + \omega_j = \omega_l + \omega_m$:

$$\frac{dA_i}{dt} = -\gamma_i A_i - \frac{2}{\gamma_g} \sum_{j,l,m=1}^{M} \kappa_{ij}\kappa_{lm} A_j^\dagger A_l A_m + 2\sum_{j=1}^{M} A_j^\dagger \eta_g e^{i(\omega_i+\omega_j)t} + \eta_i e^{i\omega_i t} - \int_0^L \sigma_i^* e^{i\omega_i t} S_-(z)\sin(K_i z)dz. \tag{A19}$$

Now we turn to the two level system equations of motion. Although the Nd:YAG laser is actually a four level system, this model works well for determining the equations of motion. It fails when computing the spontaneous emission noise power, so we compute this power in another way. In the meanwhile we will ignore all noise contributions from the two level system.

The pertinent equations of motion are

$$\frac{dS_3(z)}{dt} = 2\sum_{i=1}^{M} \sigma_i [S_+(z)a_i + a_i^\dagger S_-(z)]\sin(K_i z) + 2\sum_k [\Gamma_{sk}(z)S_+(z)b_{sk} + \Gamma_{sk}^*(z)b_{sk}^\dagger S_-(z)] + 2\Lambda, \tag{A20}$$

$$\frac{dS_+(z)}{dt} = i\omega_s S_+(z) - \sum_k \Gamma_{sk}^*(z) b_{sk}^\dagger S_3(z) - \sum_{i=1}^{M} \sigma_i a_i^\dagger S_3(z)\sin(K_i z), \tag{A21}$$

$$\frac{dS_-(z)}{dt} = -i\omega_s S_-(z) - \sum_k \Gamma_{sk}(z) S_3(z) b_{sk} - \sum_{i=1}^{M} \sigma_i S_3(z) a_i \sin(K_i z), \tag{A22}$$

$$\frac{db_{sk}}{dt} = -i\Omega_{sk} b_{sk} - \int_0^L \Gamma_{sk}^*(z) S_-(z)dz, \tag{A23}$$

$$\frac{db_{sk}^\dagger}{dt} = i\Omega_{sk} b_{sk}^\dagger - \int_0^L \Gamma_{sk}(z) S_+(z)dz. \tag{A24}$$

Note that we have added a constant 2Λ to the S_3 equation to account for the steady-state population inversion due to optical pumping. Λ is a pumping rate density and has units of $1/(\text{length} \times \text{time})$.

Formally integrating the reservoir operators, substituting them into the $S_+(z)$ equation of motion, and making the Langevin approximation we get

$$\frac{dS_+(z)}{dt} = (-\gamma_p + i\omega_s)S_+(z) + \eta_s(z)S_3(z) - \sum_{i=1}^{M} \sigma_i^* a_i^\dagger S_3(z)\sin(K_i z). \tag{A25}$$

At this point, we need to note that the Nd:YAG laser is a class B laser and its polarization decay rate is much higher than γ_s because the polarization of the active medium is affected by the surrounding crystal lattice. For Nd:YAG, γ_s^{-1} is approximately 240 μs. The actual polarization decay time γ_p^{-1} is on the order of 10^{-11} s. So we substitute the faster decay rate γ_p for γ_s and ignore the associated fluctuations.

Now we transform the $S_+(z)$ equation to a rotating frame with the driving term frequency ω_d by substituting

$$\mathcal{S}_+(z) = e^{-i\omega_d t} S_+(z), \tag{A26}$$

$$\frac{d\mathcal{S}_+(z)}{dt} = [-\gamma_p + i(\omega_s - \omega_d)]\mathcal{S}_+(z) - \sum_{i=1}^{M} \sigma_i a_i^\dagger e^{-i\omega_d t} S_3(z)\sin(K_i z). \tag{A27}$$

Since the polarization decay rate is so high, the $\mathcal{S}_+(z)$ equation is slaved to the population $S_3(z)$ and the field $a_i e^{i\omega_d t}$. So we adiabatically eliminate this equation by setting

$$\frac{d\mathcal{S}_+(z)}{dt}=0. \tag{A28}$$

We also assume $\gamma_p >> \omega_s-\omega_d$, which is equivalent to saying that the modes that lase are very near the peak of the Lorentzian line shape of the transition. The $\mathcal{S}_-(z)$ equation is similar.

$$\mathcal{S}_+(z)=-\frac{1}{\gamma_p}\sum_{i=1}^{M}\sigma_i a_i^\dagger e^{-i\omega_d t}\sin(K_i z)S_3(z), \tag{A29}$$

$$\mathcal{S}_-(z)=-\frac{S_3(z)}{\gamma_p}\sum_{i=1}^{M}\sigma_i a_i e^{i\omega_d t}\sin(K_i z). \tag{A30}$$

We now take the $S_3(z)$ equation, substitute the reservoir solutions, and perform the Langevin approximations:

$$\begin{aligned}\frac{dS_3(z)}{dt}=&2\Lambda-2\gamma_s[I+S_3(z)]-2[S_+(z)\eta_s^\dagger(z)\\&-\eta_s(z)S_-(z)]+2\sum_{i=1}^{M}\sigma_i[S_+(z)a_i\\&+a_i^\dagger S_-(z)]\sin(K_i z).\end{aligned} \tag{A31}$$

For simplicity, we ignore the noise contribution term $\eta_s(z)$. Substituting $\mathcal{S}_\pm(z)e^{\pm i\omega_d t}$ for $S_\pm(z)$, assuming $S_3(z)$ commutes with a_i, and ignoring cross terms we have

$$\begin{aligned}\frac{dS_3(z)}{dt}=&2\Lambda-2\gamma_s[I+S_3(z)]-\frac{1}{\gamma_p}S_3(z)\\&\times\sum_{i=1}^{M}\sigma_i^2 a_i^\dagger a_i\sin^2(K_i z).\end{aligned} \tag{A32}$$

We substitute in A_i and multiply the entire equation by N, the total number of atoms.

$$\begin{aligned}\frac{dNS_3(z)}{dt}=&2N\Lambda-2\gamma_s[NI+NS_3(z)]-\frac{4}{\gamma_p}NS_3(z)\\&\times\sum_{i=1}^{M}\sigma_i^2 A_i^\dagger A_i\sin^2(K_i z).\end{aligned} \tag{A33}$$

Associating the operator $NS_3(z)$ with the population inversion $n(z)$, we find that NI must be the density of two level systems in the medium N/L. We also define

$$\tau_f\equiv(2\gamma_s)^{-1}, \tag{A34}$$

$$\overline{n}\equiv\left[\frac{N\Lambda}{\gamma_s}-\frac{N}{L}\right] \tag{A35}$$

to get

$$\frac{dn(z)}{dt}=-\frac{1}{\tau_f}(n(z)-\overline{n})-n(z)\sum_{i=1}^{M}4\frac{\sigma_i^2}{\gamma_p}A_i^\dagger A_i\sin^2(K_i z), \tag{A36}$$

where τ_f is the fluorescence decay time of the Nd:YAG medium (240 μs) and $\overline{n}$ is the mean population inversion.

Now we return to the field equation and substitute $\mathcal{S}_-(z)e^{-i\omega_d t}$ for $S_-(z)$ and take advantage of the orthogonality condition of the normal modes

$$\int_0^L\sin(K_i z)\sin(K_j z)dz=\delta_{ij} \tag{A37}$$

to get

$$\begin{aligned}\frac{dA_i}{dt}=&-\gamma_i A_i-\frac{2}{\gamma_g}\sum_{j,l,m=1}^{M}\kappa_{ij}\kappa_{lm}A_j^\dagger A_l A_m\\&+2\sum_{j=1}^{M}A_j^\dagger\eta_g e^{i(\omega_i+\omega_j)t}+\eta_i e^{i\omega_i t}\\&+\frac{\sigma_i^2}{N\gamma_p}\int_0^L\sin^2(K_i z)n(z)dzA_i.\end{aligned} \tag{A38}$$

We have identified $n(z)$ here. At this point we recall that the number of photons in the cavity is large (10^9) and treat the quantum mechanical operators A_i and $A_i^\dagger$ as if they are c numbers.

We break the population equation into the component normal modes as described in detail in [3]. To do this, we define a mode gain G_i as

$$G_i=\frac{2|\sigma_i|^2\tau_c}{N\gamma_p}\int_0^L n(z)\sin^2(K_i z)dz, \tag{A39}$$

where τ_c is the round trip cavity time of the laser (0.2 ns). Then

$$\begin{aligned}\frac{dG_i}{dt}=&\frac{2\sigma_i^2\tau_c}{N\gamma_p}\int_0^L\Bigg[-\frac{1}{\tau_f}[n(z)-\overline{n}]\\&-n(z)\sum_{j=1}^{M}\frac{4|\sigma_j|^2}{\gamma_p}|A_j|^2\sin^2(K_j z)\Bigg]\sin^2(K_i z)\,dz.\end{aligned} \tag{A40}$$

We integrate the first two terms on the right hand side and substitute the pumping power

$$\rho_i=\frac{\sigma_i^2\overline{nL}\tau_c}{N\gamma_p}, \tag{A41}$$

$$\begin{aligned}\frac{dG_i}{dt}=&\frac{1}{\tau_f}(\rho_i-G_i)-\frac{2\sigma_i^2\tau_c}{N\gamma_p}\sum_{j=1}^{M}2\frac{|\sigma_j|^2}{\gamma_p}A_j|^2\\&\times\int_0^L n(z)\sin^2(K_i z)dz+\frac{2\sigma_i^2\tau_c}{N\gamma_p}\sum_{j=1}^{M}2\frac{\sigma_i^2}{\gamma_p}|A_j|^2\\&\times\int_0^L n(z)\cos(2K_j z)\left(\frac{1-\cos(2K_i z)}{2}\right)dz.\end{aligned} \tag{A42}$$

We define the mode coupling constant ξ_{ij}:

$$\xi_{ij}=\frac{\int_0^L n(z)\cos(2K_j z)[1-\cos(2K_i z)]dz}{\int_0^L n(z)[1-\cos(2K_i z)]dz}$$

$$= \frac{\int_0^L n(z)\cos(2K_j z)[1-\cos(2K_i z)]dz}{2G_i(N\gamma_p/2\sigma_i^2\tau_c)} \tag{A43}$$

This coefficient is truly a constant if $n(z,t)$ factors into separate time and space dependent components; this is probably a good assumption for a standing wave cavity. Thus

$$\frac{dG_i}{dt} = \frac{1}{\tau_f}(\rho_i - G_i) - G_i \sum_{j=1}^{M} \frac{2|\sigma_j|^2}{\gamma_p}|A_j|^2 + G_i \sum_{j=1}^{M} \frac{2|\sigma_j|^2}{\gamma_p}|A_j|^2 \xi_{ij} \tag{A44}$$

$$= \frac{1}{\tau_f}\left[\rho_i - G_i\left(1 + \sum_{j=1}^{M} \beta'_{ij}|A_j|^2\right)\right], \tag{A45}$$

where

$$\beta'_{ij} = \frac{2\sigma_i^2}{\gamma_p}\tau_f(1-\xi_{ij}). \tag{A46}$$

The field equation is simplified.

$$\frac{dA_i}{dt} = \left(\frac{G_i}{2\tau_c} - \gamma_i\right)A_i - \frac{2}{\gamma_g}\sum_{j,l,m=1}^{M} \kappa_{ij}\kappa_{lm}A_j^\dagger A_l A_m + 2\sum_{j=1}^{M} \kappa_j A_j^\dagger \eta_g e^{i(\omega_i+\omega_j)t} + \eta_i e^{i\omega_i t}. \tag{A47}$$

We rescale the field equation so that it has measurable units. We define the electric field E so that $I=|E|^2$ has units of watts. That is,

$$|E_i|^2 = |A_i|^2 \frac{\hbar\omega_d}{\tau_c} \tag{A48}$$

since $|A_i|^2$ is simply the number of photons in mode i. We also substitute $\alpha_i = 2\gamma_i\tau_c$ and assume the κ_{ij} are real:

$$\frac{dE_i}{dt} = \frac{1}{2\tau_c}\left[(G_i-\alpha_i)E_i - \frac{4\tau_c^2}{\hbar\omega_d\gamma_g}\sum_{j,l,m=1}^{M} \kappa_{ij}\kappa_{lm}E_j^* E_l E_m\right] + 2\sum_{j=1}^{M} \kappa_{ij}E_j^* \eta_g e^{i(\omega_i+\omega_j)t} + \sqrt{\frac{\hbar\omega_d}{\tau_c}}\eta_i e^{i\omega_i t}. \tag{A49}$$

Now we define κ and ζ_{ij} so that $\kappa\zeta_{ij}=\kappa_{ij}$ and ζ_{ij} is unitless and of order unity and define

$$\epsilon = \frac{4\tau_c^2\kappa^2}{\hbar\omega_d\gamma_g}, \tag{A50}$$

which has units of inverse watts. We also define

$$\beta_{ij} = \beta'_{ij}\frac{\hbar\omega_d}{\tau_c} = \frac{2|\sigma_i|^2\hbar\omega_d\tau_f}{\gamma_p\tau_c}(1-\xi_{ij}) \tag{A51}$$

which has units of inverse watts. The resulting equations are

$$\frac{dE_i}{dt} = \frac{1}{2\tau_c}\left[(G_i-\alpha_i)E_i - \epsilon\sum_{j,k,l=1}^{M} \zeta_{ij}\zeta_{lm}E_j^* E_l E_m\right] + 2\kappa\sum_{j=1}^{M} \zeta_{ij}E_j^* \eta_g e^{i(\omega_i+\omega_j)t} + \sqrt{\frac{\hbar\omega_d}{\tau_c}}\eta_i e^{i\omega_i t}, \tag{A52}$$

$$\frac{dG_i}{dt} = \frac{1}{\tau_f}\left[\rho_i - G_i\left(1 + \sum_{j=1}^{M} \beta_{ij}|E_j|^2\right)\right]. \tag{A53}$$

[1] T. Baer, J. Opt. Soc. Am. B **3**, 1175 (1986).

[2] C. Bracikowski, and R. Roy, Chaos **1**, 49 (1991).

[3] R. Roy, C. Bracikowski, and G.E. James, in *Proceedings of the International Conference on Int. Conf. Quantum Optics*, edited by R. Inguva and G. S. Agarwal (Plenum Press, New York, 1992).

[4] R. Roy, T. W. Murphy, Jr., T. D. Maier, Z. Gills, and E. R. Hunt, Phys. Rev. Lett. **68**, 1259 (1992).

[5] Z. Gills, C. Iwata, R. Roy, I. B. Schwartz, and I. Triandaf, Phys. Rev. Lett. **69**, 3169 (1992).

[6] P. Colet, R. Roy, and K. Wiesenfeld, Phys. Rev. E **50**, 3453 (1994).

[7] T. W. Carr and I. B. Schwartz, Phys. Rev. E **51**, 5109 (1995).

[8] H. D. I. Abarbanel, Z. Gills, C. Liu, and R. Roy, Phys. Rev. A **53**, 440 (1996).

[9] H. D. I. Abarbanel, R. Brown, J. J. Sidorowich, and Lev Sh. Tsimring, Rev. Mod. Phys. **65**, 1331 (1993).

[10] H. D. I. Abarbanel, *Analysis of Observed Chaotic Data* (Springer, New York, 1996).

[11] R. Mañé, in *Dynamical Systems and Turbulence, Warwick 1980*, edited by D. Rand and L. S. Young, Lecture Notes in Mathematics Vol. 898 (Springer, Berlin, 1981), p. 230.

[12] F. Takens, in *Dynamical Systems and Turbulence, Warwick 1980*, edited by D. Rand and L. S. Young, Lecture Notes in Mathematics Vol. 898 (Springer, Berlin, 1981), p. 366.

[13] (a) A. M. Fraser and H. L. Swinney, Phys. Rev. A **33**, 1134 (1986); (b) A. M. Fraser, IEEE Trans. Inf. Theory **35**, 245 (1989).

[14] Matthew B. Kennel, R. Brown, and H. D. I. Abarbanel, Phys. Rev. A **45**, 3403 (1992).

[15] M. Sargent III, M. O. Scully, and W. E. Lamb, Jr., *Laser Physics* (Addison-Wesley, Reading, MA, 1974).

[16] A. Yariv, *Quantum Electronics*, 3rd ed. (Wiley, New York, 1989).

[17] P. D. Drummond, K. J. McNiel, and D. F. Walls, Opt. Acta **28**, 211 (1981).

[18] D. F. Walls and G. J. Milburn, *Quantum Optics* (Springer, Berlin, 1994).